Astronomy & Astrophysics manuscript no. output
March 14, 2024

A deep search for large complex organic species toward IRAS16293-2422 B at 3 mm with ALMA

P. Nazari[1], J. S. Y. Cheung[2], J. Ferrer Asensio[3], N. M. Murillo[4,5], E. F. van Dishoeck[1,3], J. K. Jørgensen[6], T. L. Bourke[7], K. -J. Chuang[8], M. N. Drozdovskaya[9], G. Fedoseev[10], R. T. Garrod[11], S. Ioppolo[12], H. Linnartz[8], B. A. McGuire[2,13], H. S. P. Müller[14], D. Qasim[15], and S. F. Wampfler[9]

(Affiliations can be found after the references)

Received 30 August 2023 / Accepted 13 December 2023

ABSTRACT

Context. Complex organic molecules (COMs) have been detected ubiquitously in protostellar systems. However, at shorter wavelengths (∼0.8 mm), it is generally more difficult to detect larger molecules than at longer wavelengths (∼3 mm) because of the increase in millimeter dust opacity, line confusion, and unfavorable partition function.

Aims. We aim to search for large molecules (more than eight atoms) in the Atacama Large Millimeter/submillimeter Array (ALMA) Band 3 spectrum of IRAS 16293-2422 B. In particular, the goal is to quantify the usability of ALMA Band 3 for molecular line surveys in comparison to similar studies at shorter wavelengths.

Methods. We used deep ALMA Band 3 observations of IRAS 16293-2422 B to search for more than 70 molecules and identified as many lines as possible in the spectrum. The spectral settings were set to specifically target three-carbon species such as i- and n-propanol and glycerol, the next step after glycolaldehyde and ethylene glycol in the hydrogenation of CO. We then derived the column densities and excitation temperatures of the detected species and compared the ratios with respect to methanol between Band 3 (∼3 mm) and Band 7 (∼1 mm, Protostellar Interferometric Line Survey) observations of this source to examine the effect of the dust optical depth.

Results. We identified lines of 31 molecules including many oxygen-bearing COMs such as CH_3OH, CH_2OHCHO, CH_3CH_2OH, and c-C_2H_4O and a few nitrogen- and sulfur-bearing ones such as $HOCH_2CN$ and CH_3SH. The largest detected molecules are gGg-$(CH_2OH)_2$ and CH_3COCH_3. We did not detect glycerol or i- and n-propanol, but we do provide upper limits for them which are in line with previous laboratory and observational studies. The line density in Band 3 is only ∼2.5 times lower in frequency space than in Band 7. From the detected lines in Band 3 at a $\gtrsim 6\sigma$ level, ∼25 – 30% of them could not be identified indicating the need for more laboratory data of rotational spectra. We find similar column densities and column density ratios of COMs (within a factor ∼2) between Band 3 and Band 7.

Conclusions. The effect of the dust optical depth for IRAS 16293-2422 B at an off-source location on column densities and column density ratios is minimal. Moreover, for warm protostars, long wavelength spectra (∼3 mm) are not only crowded and complex, but they also take significantly longer integration times than shorter wavelength observations (∼0.8 mm) to reach the same sensitivity limit. The 3 mm search has not yet resulted in the detection of larger and more complex molecules in warm sources. A full deep ALMA Band 2 – 3 (i.e., ∼3 – 4 mm wavelengths) survey is needed to assess whether low frequency data have the potential to reveal more complex molecules in warm sources.

Key words. Astrochemistry – Stars: low-mass – Stars: protostars – ISM: abundances – ISM: molecules

1. Introduction

In the interstellar medium (ISM) complex organic molecules (COMs), defined as species with at least six atoms containing carbon (Herbst & van Dishoeck 2009), are particularly prominent in the protostellar phase. Although other phases of star formation such as the prestellar phase (e.g., Bacmann et al. 2012; Jiménez-Serra et al. 2016; McGuire et al. 2020; Scibelli & Shirley 2020) and the later protoplanetary disk phase (Öberg et al. 2015; Walsh et al. 2016; Booth et al. 2021; Brunken et al. 2022) show detections of these species, COMs are more easily detectable in the line-rich protostellar envelopes due to their higher temperatures (e.g., Blake et al. 1987; Belloche et al. 2013; Bergner et al. 2017; van Gelder et al. 2020; Nazari et al. 2021; Yang et al. 2021; McGuire 2022; Bianchi et al. 2022; Hsu et al. 2022).

Many COMs, including species with more than eight atoms, are expected to form in ices under laboratory conditions (ethanol – CH_3CH_2OH, Öberg et al. 2009; Chuang et al. 2020; Fedoseev et al. 2022; aminomethanol – NH_2CH_2OH, Theulé et al. 2013; glycerol – $HOCH_2CH(OH)CH_2OH$, Fedoseev et al. 2017; 1-propanol – $CH_3CH_2CH_2OH$, Qasim et al. 2019a,b; glycine – NH_2CH_2COOH, Ioppolo et al. 2021). However, there is a lot of debate regarding the ice or gas-phase formation of particular COMs (e.g., Ceccarelli et al. 2022). Two examples of these species are formamide (NH_2CHO) and acetaldehyde (CH_3CHO) for which both gas and ice formation pathways are suggested (e.g., Jones et al. 2011; Barone et al. 2015; Vazart et al. 2020; Chuang et al. 2020, 2021, 2022; Fedoseev et al. 2022; Garrod et al. 2022). To obtain clues as to the formation mechanism of COMs from an observational perspective, it is possible to search for the solid state signatures of COMs in ices (Schutte et al. 1999; Öberg et al. 2011) with telescopes such as the *James Webb Space Telescope* (Yang et al. 2022; McClure et al. 2023; Rocha et al. in prep.) using laboratory spectra available from, for example, the Leiden Ice Database for Astrochemistry (Rocha et al. 2022) and to examine the gas-phase correlations between different COMs in large samples of sources (Belloche et al. 2020; Coletta et al. 2020; Jørgensen et al. 2020; Nazari et al. 2022a; Taniguchi et al. 2023; Chen et al. 2023). However, observations and models show that physical effects such as the source structure or dust optical depth could affect the snowline locations,

Article published by EDP Sciences, to be cited as https://doi.org/10.1051/0004-6361/202347832

gas-phase emission, and column density correlations of simple and complex molecules (Jørgensen et al. 2002; Persson et al. 2016; De Simone et al. 2020; Nazari et al. 2022b; Murillo et al. 2022a; Nazari et al. 2023a,b). Hence, interpretations of COM formation routes based on gas-phase observations can be affected by these physical factors. For example, an anticorrelation between column densities of two species (or a large scatter in the column density ratios) could have a physical origin rather than a chemical origin.

Among the low-mass protostars, the IRAS16293-2422 (IRAS16293 hereafter) triple protostellar system (Wootten 1989; Maureira et al. 2020) is one of the closest protostars, and one of the richest and most well-studied objects from a chemical perspective. The first detection of methanol (CH_3OH; the simplest COM) toward a low-mass protostar was carried out by van Dishoeck et al. (1995) for this system. Since then, its chemistry and in particular the COMs in this system have been studied in more detail (Cazaux et al. 2003; Butner et al. 2007; Bisschop et al. 2008; Ceccarelli et al. 2010; Jørgensen et al. 2011; Jørgensen et al. 2012; Kahane et al. 2013; Jaber et al. 2014). More recently, the Protostellar Interferometric Line Survey (PILS; Jørgensen et al. 2016) studied IRAS16293 in Band 7 (~329.147 − 362.896 GHz) of the Atacama Large Millimeter/submillimeter Array (ALMA). This survey detected many COMs for the first time in the ISM, adding further information on complexity in space (Coutens et al. 2016; Lykke et al. 2017; Calcutt et al. 2018a; Jørgensen et al. 2018; Manigand et al. 2019; Manigand et al. 2021; Coutens et al. 2022).

However, a limitation of higher-frequency observations of ALMA (~330 GHz) is the higher degree of line blending. The reason is that for observations probing the same gas, the line width – although constant in velocity space – increases in frequency space (Jørgensen et al. 2020). Therefore, the detection of larger COMs with more than eight atoms, which have relatively weak lines, is expected to be easier at lower frequencies. Moreover, the heavier molecules have their Boltzmann distribution peak at lower frequencies than the lighter molecules at the same excitation temperature, and thus their lines are stronger at lower frequencies and they are more easily detected at long wavelength observations. On the other hand, the Boltzmann peak moves to the higher frequencies for higher temperatures (see Fig. 2 of Herbst & van Dishoeck 2009). Therefore, if the large molecules are thermally sublimated in the inner hot regions around the protostar (tracing warm or hot regions), it is difficult to observe these larger species even at low frequencies (although favored), unless the data are sensitive enough, which can be achieved at the expense of the angular resolution and longer integration times. The combination of the increase in line width in frequency space and the Boltzmann distribution peak of the lighter molecules being at higher frequencies also lead to spectra being more crowded, and thus it is more difficult to detect large molecules at high frequencies.

Moreover, dust optical depth effects could be an important issue at higher-frequency ALMA Bands 6 (~240 GHz) and 7 (~330 GHz). This is because of the larger dust opacity of ~1 mm-sized grains at shorter wavelengths (i.e, higher frequencies). For example, López-Sepulcre et al. (2017) found that NGC 1333 IRAS 4A1 in Perseus does not host any COMs when searched for with ALMA and the Plateau de Bure Interferometer. However, later, De Simone et al. (2020) detected methanol around this source at longer wavelengths with the Very Large Array (VLA). Another example is the ring-shaped structure of methanol around the dust continuum in the massive protostellar system 693050 (also known as G301.1364-00.2249) observed by van Gelder et al. (2022b) at ~220 GHz with ALMA, which indicates dust attenuation on-source.

For this work, we used the deep Band 3 ALMA observations of IRAS16293 B to search for larger species (more than eight atoms). This dataset was specifically optimized to hunt for molecules such as glycerol and i- and n-propanol. Although the main aim is to specifically hunt for large molecules, we identified as many molecules as possible from the Cologne Database for Molecular Spectroscopy (CDMS; Müller et al. 2001; Müller et al. 2005) and the Jet Propulsion Laboratory database (JPL; Pickett et al. 1998) in our data. We fit the spectrum to derive the column densities and excitation temperatures of the detected species and we compared our results with those of PILS in Band 7. In particular, we examined whether dust attenuation is important for column densities and their ratios with respect to methanol (typically used as a reference species).

The paper is structured such that the observations are explained in Sect. 2. The results including the detected species and their column densities and excitation temperatures are given in Sect. 3. We discuss our findings, in particular the comparison with the PILS results in Sect. 4. Finally, we present our conclusions in Sect. 5.

2. Observations and methods

2.1. Data

This paper uses the data of IRAS16293 B taken with ALMA in Band 3 (project code: 2017.1.00518.S; PI: E. F. van Dishoeck). For more information on the data calibration, reduction, and imaging, as well as the first results on the gas accretion flow in the IRAS16293 system, readers can refer to Murillo et al. (2022b); here we give a brief description of the data. We used the data with the configuration C43-4, which were calibrated with the CASA pipeline (McMullin et al. 2007) and then self-calibrated with CASA. Continuum subtraction was done on the self-calibrated image datacubes using STATCONT (Sánchez-Monge et al. 2018).

The data have an angular resolution of ~0.9″×0.7″, which is larger than that of PILS (~0.5″). The frequency ranges covered were ~90.59 − 91.41 GHz (continuum), ~93.14 − 93.20 GHz, and ~103.28 − 103.52 GHz. After conversion of the flux to brightness temperature, the rms found from line-free regions in each spectral window was ~0.1 K, ~0.3 K, and 0.2 K (comparable to PILS), respectively, following a 171.7 minute on-source integration time. The spectral resolution was 0.805 $km\,s^{-1}$, 0.049 $km\,s^{-1}$, and 0.088 $km\,s^{-1}$. Given that the lines have a full width at half maximum (FWHM) of ~1 − 2 $km\,s^{-1}$, some lines are not fully resolved in the continuum window. The frequency range was optimized to cover transitions of larger species such as glycerol as well as i- and n-propanol. It also serendipitously covered transitions from other oxygen- and nitrogen-bearing COMs including glycolaldehyde (CH_2OHCHO), propanal (g-C_2H_5CHO), and glycolonitrile ($HOCH_2CN$). The spectrum of IRAS16293 B (Fig. 1) was extracted from the same 0.5″ offset position from the continuum peak of B that was used in many of the works from ALMA-PILS (α_{J2000} = $16^h32^m22^s.58$ and δ_{J2000} = $-24°28'32.8''$, Coutens et al. 2016; Jørgensen et al. 2018; Calcutt et al. 2018b). Maps of a few common species tracing cold gas structures are presented in Murillo et al. (2022b).

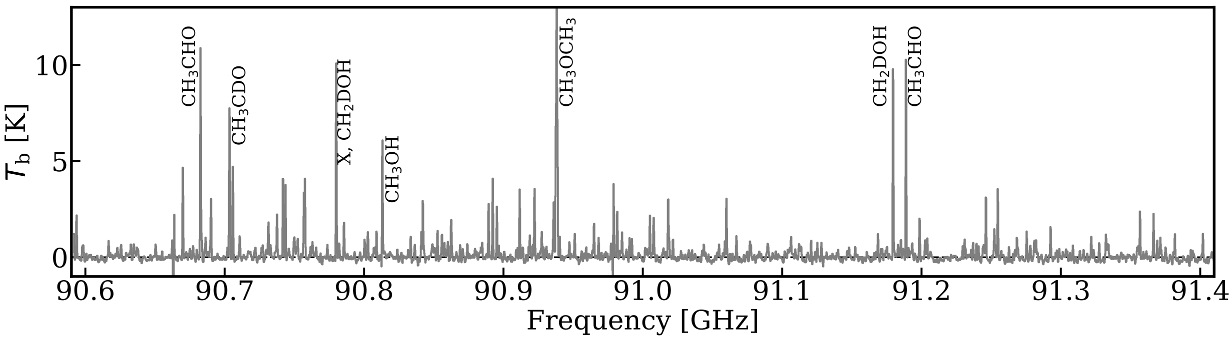

Fig. 1: Spectrum of IRAS16293 B Band 3 data for the continuum window. A few strong lines are highlighted; for the full line identification and fitting, readers can refer to Fig. B.1. We note that "X" indicates a line that has not been identified yet and that was not (fully) fitted with the considered molecules for this work. The spectrum of IRAS16293 B is line rich even at ALMA Band 3 wavelengths (∼3 mm).

2.2. Spectral modeling

For this work, we identified as many molecules as possible using the CASSIS[1] spectral analysis tool (Vastel et al. 2015). We consider a molecule as detected if it has at least three lines at a peak of the $\geq 3\sigma$ level. We also report column densities of the molecules that have one or two detected lines without any overprediction of the emission in the spectrum. These column densities are only tentative and not as robust as those found for molecules with many detected lines because of the limited frequency coverage, but they should be reliable for the most abundant and common molecules such as $^{13}CH_3OH$. Using CASSIS, we fit for the identified molecules. In the fitting procedure, the spectrum was considered as a whole; and all the lines of a molecule were fitted simultaneously assuming local thermodynamic equilibrium (LTE) conditions. The fitting followed a similar procedure as the fit-by-eye method used in Nazari et al. (2022a). This includes varying the column densities (N) and excitation temperatures (T_{ex}) in the LTE models to produce a synthetic spectrum that matches the data (for more information on this process, see below). The line lists were taken from the CDMS (Müller et al. 2001; Müller et al. 2005) or the JPL database (Pickett et al. 1998). Appendix A gives more information on the spectroscopic studies used for our assignments and Table B.2 presents the transitions covered in the data.

In the fitting process, the FWHM was first fitted for the unblended line(s) of each molecule. Then it was fixed to that value when the column density and excitation temperature were being determined. The FWHM for all considered species is $\sim 1.8 \pm 0.5\,\mathrm{km\,s^{-1}}$, except for (formic acid) t-HCOOH, which is slightly lower (i.e., $\sim 1\,\mathrm{km\,s^{-1}}$). The typical FWHM here is $\sim 1.5-2$ times larger than the typical FWHM found in PILS ($\sim 1\,\mathrm{km\,s^{-1}}$). However, the spectral resolution for the continuum spectral window (i.e., the major spectral window where most lines lie; Fig. B.1) is $\sim 0.8\,\mathrm{km\,s^{-1}}$ in this work. This implies that not all lines are spectrally resolved. Therefore, the higher FWHM measured here could be due to this low spectral resolution. The excitation temperature was only fitted if there were enough (≥ 2) detected lines of a molecule with a range of E_{up} (e.g., $\sim 100-400$ K). The typical uncertainty on the excitation temperature is $\sim \pm 50$ K. If not enough lines with a range of E_{up} were detected, the temperature is fixed to 100 K, which is similar to excitation temperatures assumed or found for many species in PILS (Lykke et al. 2017; Calcutt et al. 2018b; Jørgensen et al. 2018). The exceptions to this rule were t-HCOOH and NH_2CHO. Only one line was detected for each of these two molecules and their temperatures were fixed to 300 K to be consistent with PILS (Coutens et al. 2016; Jørgensen et al. 2018). Moreover, for the isotopologues for which a determination of the excitation temperature was not possible, the temperature was fixed to that of the other isotopologues with a determined T_{ex}. Deuterated methanol, CH_2DOH, has three detected lines, with upper energy levels of ∼10 K, ∼100 K, and ∼400 K. It was not possible to fit all three lines of this molecule with a single excitation temperature. Therefore, we adopted the same temperature as the methanol isotopologue that has the most lines detected (i.e., CHD_2OH). However, this temperature fits the ∼100 K line better than the other two. For aGg′-$(CH_2OH)_2$, we note that again a single temperature cannot fit all of its lines. In particular, the line at 90.593 GHz with $E_{up} = 19$ K gets overestimated regardless of the temperature assumed. This could be because of this line being (marginally) optically thick; therefore, we ignored this line and fixed the temperature to that of gGg′-$(CH_2OH)_2$. A similar two-component temperature structure was found for glycolonitrile ($HOCH_2CN$) toward IRAS 16293 B (Zeng et al. 2019). Using this method the rest of the lines are explained reasonably well (i.e., within $\sim 20-30\%$; see Fig. B.1).

The column density was always treated as a free parameter. The uncertainty on column densities was measured from the same method explained in Nazari et al. (2022a) and the typical uncertainty from the fits is on the order of 20%. Figure B.1 shows the final fitted model for each molecule. As this figure shows, there are still unidentified lines in the spectrum (see Sect. 3.1 for more details). In this process, the source velocity was fixed to $V_{lsr} = 2.7\,\mathrm{km\,s^{-1}}$ and a beam dilution of unity was assumed resulting in our column densities being representative of those within a beam. This is different from the assumption in PILS where the source size was set to 0.5″. Nevertheless, this assumption does not change the conclusions as long as the lines are optically thin. This is because only the number of molecules and their ratios are of interest here. The number of molecules ($\mathcal{N}$) is constant regardless of the source size assumed. The number of molecules is equal to $N \times A$, where A is the emitting area. Hence a decrease in the emitting area increases the fitted column densities and vice versa such that the number of molecules stays the same as long as the lines stay optically thin (also see van Gelder et al. 2022a; Nazari et al. 2023c). However, we note that

[1] http://cassis.irap.omp.eu/

with this assumption, we ignored any potential differences between the emitting areas of various molecules. This assumption can only be improved with higher angular resolution data than presented in this work.

3. Results

3.1. Deep search and the considered species

The spectrum of IRAS16293 B at ~3 mm wavelengths is line rich and crowded (see Fig. 1 for an overview). In total, 16 molecules were detected and 15 were tentatively detected (see Table 1). Ratios of the detected molecules with respect to methanol are presented in the left panel of Fig. 2 (see Sect. 4.2.3 for a discussion on the comparison with PILS). Among these species, many "standard" COMs such as methanol (CH_3OH), ethanol (CH_3CH_2OH), ethyl cyanide (CH_3CH_2CN), acetaldehyde (CH_3CHO), methyl formate (CH_3OCHO), and dimethyl ether (CH_3OCH_3) with some of their isotopologues are apparent. The frequency range did not cover transitions of CH_3CN and HNCO or their isotopologues. We also detected one carbon chain molecule, cyanoacetylene (HCCCN). It should be noted that the frequency range of the observations covers HC_5N transitions, but this carbon chain was not detected toward IRAS16293 B. It was, however, detected ~12″ off-source to the west of IRAS16293 B (Murillo et al. 2022b).

This dataset was specifically taken to search for large species due to the expected lower line density and line confusion in Band 3 in comparison with Band 7 used for PILS. Moreover, at the same excitation temperature, heavier molecules have their Boltzmann distribution peak at lower frequencies, which increases the chance of detecting them in Band 3. Particularly, the frequency windows were selected to search for glycerol ($HOCH_2CH(OH)CH_2OH$) and propanol (C_3H_7OH). Isopropanol (i-C_3H_7OH) and normal-propanol (n-C_3H_7OH) have been detected previously in the ISM (Belloche et al. 2022; Jiménez-Serra et al. 2022), although not yet in IRAS16293 B (Taquet et al. 2018). In addition to these molecules, we searched for and detected large and complex species such as aGg'- and gGg'-ethylene glycol ($(CH_2OH)_2$, glycolaldehyde (CH_2OHCHO), and acetone (CH_3COCH_3).

Table B.1 presents the upper limits of the molecules we searched for but do not detect, including glycerol and isopropanol. The largest molecule that we searched for is cyanonaphthalene ($C_{10}H_7CN$; McNaughton et al. 2018) and its upper limit is given in Table B.1. Figures 3, B.2, and B.3 present the lines of g-Isopropanol, Ga-n-propanol, and G′Gg′gg′-Glycerol with the model upper limits. We note that in Fig. 3, the lines that seem to agree well with the data in the first two panels are well explained with other molecules (see the cyan line as the total fitted model for the detected or tentatively detected species), and thus they could not be the lines of g-Isopropanol. Moreover, the line at around 91.345 GHz overestimates the data. The ratio of measured upper limits with respect to methanol are presented in the right panel of Fig. 2. The ratios span a range of ~5 orders of magnitude from $\sim10^{-6}$ to ~0.1, which is similar to the range seen for the detected molecules (left panel of Fig. 2).

The line density of the lines detected at $\gtrsim 6\sigma$ level in Band 3 (~100 GHz) data is one per ~8.5 MHz (see Fig. B.1 for the variations in line density across the frequency range), while the line density is one per ~3.5 MHz in Band 7 (~345 GHz; Jørgensen et al. 2016). Therefore, as expected, the spectrum has a lower line density in Band 3 than Band 7, although only by a factor of ~2.5, resulting in a relatively line-rich spectrum still. Although many lines (~70%) in the Band 3 spectrum of IRAS16293 B were identified, we could not associate any simple or complex species to ~25 – 30% of lines at the $\gtrsim 6\sigma$ level. Potentially more high-resolution laboratory spectra are needed to identify those lines. This is particularly important for the (doubly) deuterated isotopologues of known COMs and larger COMs with more than eight atoms.

Table 1: Fitted parameters for detected and tentatively detected Band 3 species toward IRAS 16293 B.

Species	N (cm^{-2})	T_{ex} (K)	N_X/N_{CH_3OH}	# Detected lines
$^{13}CH_3OH$	$1.2^{+0.4}_{-0.2}\times10^{17}$	130^{+30}_{-20}	$1.5^{+0.7}_{-0.4}\times10^{-2}$	2
CH_2DOH	$1.5^{+0.1}_{-0.3}\times10^{17}$	[170]	$1.8^{+0.6}_{-0.5}\times10^{-2}$	3
CHD_2OH	$1.9^{+0.4}_{-0.3}\times10^{17}$	170^{+40}_{-40}	$2.3^{+0.9}_{-0.6}\times10^{-2}$	9
CD_3OH	$5.6^{+0.7}_{-0.9}\times10^{16}$	[170]	$6.9^{+2.4}_{-1.8}\times10^{-3}$	1
CH_3CHO	$3.5^{+0.2}_{-0.4}\times10^{16}$	70^{+20}_{-10}	$4.3^{+1.5}_{-1.0}\times10^{-3}$	3
$^{13}CH_3CHO$	$2.1^{+0.3}_{-0.3}\times10^{15}$	[100]	$2.6^{+0.9}_{-0.7}\times10^{-4}$	2
CH_2DCHO	$4.0^{+0.5}_{-0.5}\times10^{15}$	[100]	$4.9^{+1.7}_{-1.2}\times10^{-4}$	2
CH_3CDO	$5.0^{+2.0}_{-2.0}\times10^{15}$	110^{+30}_{-30}	$6.1^{+3.2}_{-2.8}\times10^{-4}$	3
CHD_2CHO	$3.0^{+0.5}_{-0.8}\times10^{15}$	[100]	$3.7^{+1.4}_{-1.2}\times10^{-4}$	3
CH_3COOH	$1.0^{+0.6}_{-0.2}\times10^{16}$	170^{+30}_{-70}	$1.2^{+0.8}_{-0.4}\times10^{-3}$	3
CH_2OHCHO	$4.6^{+0.6}_{-0.6}\times10^{16}$	280^{+20}_{-40}	$5.6^{+2.0}_{-1.4}\times10^{-3}$	6
$^{13}CH_2OHCHO$	$\sim2.0\times10^{15}$	[280]	$\sim2.4\times10^{-4}$	2
CHDOHCHO	$2.5^{+0.8}_{-0.8}\times10^{15}$	120^{+50}_{-50}	$3.1^{+1.5}_{-1.2}\times10^{-4}$	4
CH_3CH_2OH	$6.2^{+0.8}_{-0.7}\times10^{16}$	170^{+20}_{-20}	$7.6^{+2.7}_{-1.8}\times10^{-3}$	5
a-a-CH_2DCH_2OH	$2.4^{+0.5}_{-0.3}\times10^{16}$	[170]	$3.0^{+1.1}_{-0.7}\times10^{-3}$	1
a-CH_3CHDOH	$2.1^{+0.4}_{-0.3}\times10^{16}$	[170]	$2.5^{+1.0}_{-0.6}\times10^{-3}$	3
CH_3OCH_3	$8.5^{+2.5}_{-2.5}\times10^{16}$	100^{+20}_{-20}	$1.0^{+0.5}_{-0.4}\times10^{-2}$	10
CH_3OCHO	$1.0^{+0.1}_{-0.2}\times10^{17}$	140^{+20}_{-30}	$1.2^{+0.4}_{-0.4}\times10^{-2}$	10
aGg′-$(CH_2OH)_2$	$\sim1.4\times10^{17}$	[160]	$\sim1.7\times10^{-2}$	15
gGg′-$(CH_2OH)_2$	$5.0^{+1.7}_{-1.4}\times10^{16}$	160^{+40}_{-40}	$6.1^{+2.9}_{-2.1}\times10^{-3}$	15
D_2CO	$6.9^{+0.6}_{-0.6}\times10^{15}$	[100]	$8.5^{+2.9}_{-1.9}\times10^{-4}$	1
HCCCN	$6.2^{+0.9}_{-0.8}\times10^{13}$	[100]	$7.6^{+2.8}_{-1.8}\times10^{-6}$	1
CH_3CH_2CN	$1.4^{+0.2}_{-0.1}\times10^{16}$	[100]	$1.8^{+0.7}_{-0.4}\times10^{-3}$	1
NH_2CHO	$5.6^{+1.2}_{-1.1}\times10^{16}$	[300]	$6.8^{+2.7}_{-1.9}\times10^{-3}$	1
CH_3COCH_3	$1.6^{+0.6}_{-0.5}\times10^{16}$	130^{+20}_{-20}	$2.0^{+1.0}_{-0.7}\times10^{-3}$	17
t-HCOOH	$7.7^{+1.1}_{-1.1}\times10^{16}$	[300]	$9.5^{+3.4}_{-2.4}\times10^{-3}$	1
c-C_2H_4O	$5.5^{+0.7}_{-0.5}\times10^{15}$	[100]	$6.7^{+2.4}_{-1.5}\times10^{-4}$	2
c-C_2H_3DO	$1.2^{+0.2}_{-0.2}\times10^{15}$	[100]	$1.5^{+0.5}_{-0.4}\times10^{-4}$	2
CH_3SH	$4.5^{+0.5}_{-0.7}\times10^{15}$	[100]	$5.5^{+1.9}_{-1.4}\times10^{-4}$	2
$HOCH_2CN$	$1.0^{+0.1}_{-0.1}\times10^{15}$	[100]	$1.2^{+0.4}_{-0.3}\times10^{-4}$	2

Notes. Measured column densities toward the 0.5″offset position from B in a ~1″ beam. If a source size of 0.5″ was assumed, these column densities would increase by a factor of five (i.e., $\frac{0.5^2+1^2}{0.5^2}$). The major isotopologue of methanol was detected, but its column density was calculated by scaling the $^{13}CH_3OH$ column density by $^{12}C/^{13}C$ = 68 (Milam et al. 2005). The FWHM for all molecules is $\sim1.8\pm0.5$ km s^{-1}. Species whose excitation temperature is fixed have their temperature given in square brackets. The right-most column gives an estimate of the number of relatively unblended lines that were detected for each molecule. Those detected with only one line should be taken with caution. However, we note that all of these species are detected in PILS (see the text for references).

3.2. Fitting results for the detected species

Derived column densities and excitation temperatures are given in Table 1. The measured excitation temperatures span a range

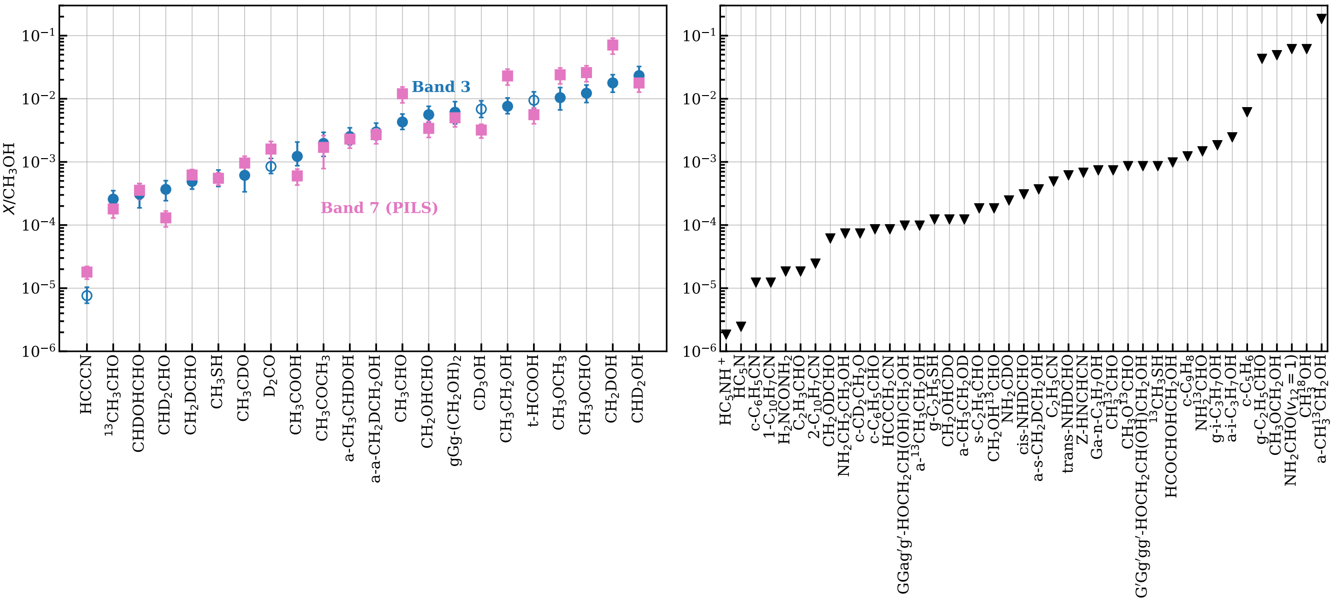

Fig. 2: Column density ratios of detected species and upper limits with respect to methanol. Left: Column density ratios for the detected species with respect to methanol for our Band 3 data (blue). The same ratios from PILS in Band 7 (pink) are also shown for comparison (see the text for references). The hollow symbols show the species that only have one detected line. Right: Ratios of the upper limits measured in this work (Table B.1) with respect to methanol. In both panels, the species are ordered from left to right by increasing Band 3 ratios with respect to methanol.

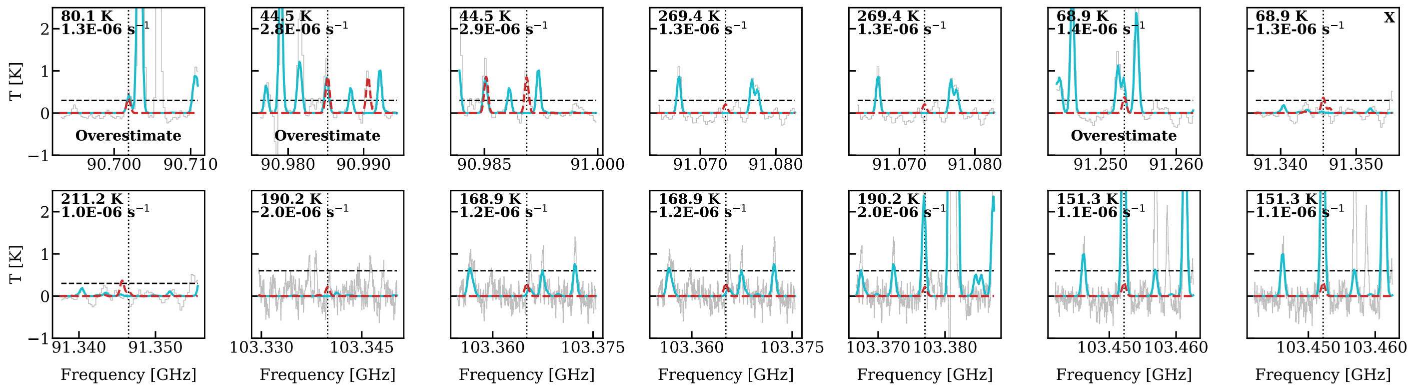

Fig. 3: Lines of g-Isopropanol and the model for its upper limit in red dashed lines (1.5×10^{16} cm^{-2}). Gray is the data and cyan is the total fitted model from the detected and tentatively detected species. The vertical dotted lines show the transition frequency of each line. The E_{up} and A_{ij} are printed in the top left of each panel. The line that was used to find the 3σ upper limit is indicated by an "X" in the top right. The horizontal dashed lines show the 3σ level. Only lines with $A_{ij} > 10^{-6}$ s^{-1} and $E_{up} < 300$ K are shown.

between ~50 and ~300 K. Figure B.4 presents the excitation temperatures where a determination was possible for molecules with sufficient detected lines. The species on the x-axis are roughly ordered by increasing binding energies in the ice from left to right (Minissale et al. 2022; Ligterink & Minissale 2023). The error bars are too large to robustly confirm whether there is any correlation between the excitation temperature and binding energy.

The column densities measured here span a range of ~4 orders of magnitude. The most abundant molecule is methanol, after that (and its isotopologues), CH_3OCHO and CH_3OCH_3 were found to be the second and third most abundant species as found in many other protostellar systems (Coletta et al. 2020; Chen et al. 2023). The column density of CH_3OH was determined by scaling the $^{13}CH_3OH$ column density by $^{12}C/^{13}C$ of 68 (Milam et al. 2005) and was found to be 8.2×10^{18} cm^{-2} in the ~1″ beam. We note that the $^{13}CH_3OH$ lines used for measurement of column density of this molecule are relatively weak and hence optically thin. They either have a large E_{up}(~500 K) or a low A_{ij} (~6×10^{-8} s^{-1}). Therefore, $^{13}CH_3OH$ in this study should robustly determine the column density of the major isotopologue without the need for $CH_3^{18}OH$. The least abundant molecule at the 0.5″ offset location is HCCCN with a column density of 6.2×10^{13} cm^{-2} (see Murillo et al. 2022b for its map).

3.3. Glycolonitrile and ethylene oxide

Here we focus on the tentative detection of $HOCH_2CN$ (glycolonitrile) and c-C_2H_4O (ethylene oxide). These two molecules are among the less common species studied toward protostars in Table 1. Glycolonitrile is an interesting interstellar molecule to study given that it is a rarely observed prebiotic molecule. Ethylene oxide is an interesting molecule because it is the only species in Table 1 with a cyclic structure.

Glycolonitrile was detected toward IRAS 16293 B using lower frequency ($\lesssim$ 266 GHz) observations than PILS (Zeng et al. 2019). Later it was also detected in PILS by Ligterink et al. (2021), mainly toward the half-beam offset position (∼0.25″ offset from the continuum peak) and not the full-beam offset position (0.5″ offset). It is interesting that in the Band 3 data, $HOCH_2CN$ was tentatively detected toward the full-beam offset position of PILS. This could be due to the larger beam size of the Band 3 observations and the inclusion of the hotter gas close to the protostar in the beam given that the binding energy of this molecule is relatively high (∼10 400 K; Ligterink & Minissale 2023).

Our tentative column density ratio of $HOCH_2CN/CH_3OH$ (∼10^{-4}) agrees well with what Ligterink et al. (2021) found for this source in Band 7. Moreover, our column density for $HOCH_2CN$, after correction for beam dilution (see Sect. 4.2.2), is within a factor of about two of what Zeng et al. (2019) found for their warm component of the same source from their Band 3 data. Moreover, glycolonitrile has been (tentatively) detected toward other objects such as the Serpens SMM1-a protostar and the G+0.693-0.027 molecular cloud with similar $HOCH_2CN/CH_3OH$ ratios of a few 10^{-4} (Requena-Torres et al. 2006; Ligterink et al. 2021; Rivilla et al. 2022). A recent study searched for its minor isotopologues in IRAS16293B and SMM1-a, but it resulted in non-detections (Margulès et al. 2023).

Ethylene oxide has been detected toward several objects, mainly high-mass protostars, but also pre-stellar cores and the comet 67P (Dickens et al. 1997; Nummelin et al. 1998; Ikeda et al. 2001; Requena-Torres et al. 2008; Bacmann et al. 2019; Drozdovskaya et al. 2019). This molecule has also been detected toward IRAS16293 A and B by PILS (Lykke et al. 2017; Manigand et al. 2020). The ratio for ethylene oxide to methanol from this work is $\sim 7 \times 10^{-4}$, which agrees well with the ratio from PILS of $\sim 3-6 \times 10^{-4}$ (Lykke et al. 2017; Jørgensen et al. 2016, 2018). Its deuterated species were studied and detected toward IRAS16293 B by Müller et al. (2023a,b). We also tentatively detected one of its deuterated species, c-C_2H_3DO, in our Band 3 data. The ratio of this molecule with respect to methanol in our data is $\sim 1-2 \times 10^{-4}$ which agrees well with the same ratio in PILS ($\sim 9 \times 10^{-5}$; Jørgensen et al. 2018; Müller et al. 2023a).

4. Discussion

4.1. Dust optical depth

For this section we calculated the continuum optical depth at ∼348.815 GHz (corresponding to ALMA Band 7) and at ∼91 GHz (corresponding to ALMA Band 3). The continuum optical depth as a zeroth-order approximation is given by (see Rivilla et al. 2017 and van Gelder et al. 2022b)

$$\tau_\nu = -\ln\left(1 - \frac{F_\nu}{\Omega_{\rm beam} B_\nu(T_{\rm dust})}\right), \quad (1)$$

where F_ν is the continuum flux density within the beam, $\Omega_{\rm beam} = \pi\theta_{\rm min}\theta_{\rm maj}/(4\ln(2))$ is the beam solid angle with $\theta_{\rm min}$ and $\theta_{\rm maj}$ as the beam minor and major axes, B_ν is the Planck function, and $T_{\rm dust}$ is the dust temperature. We took the continuum image of the PILS survey at ν∼348.815 GHz from the ALMA archive and

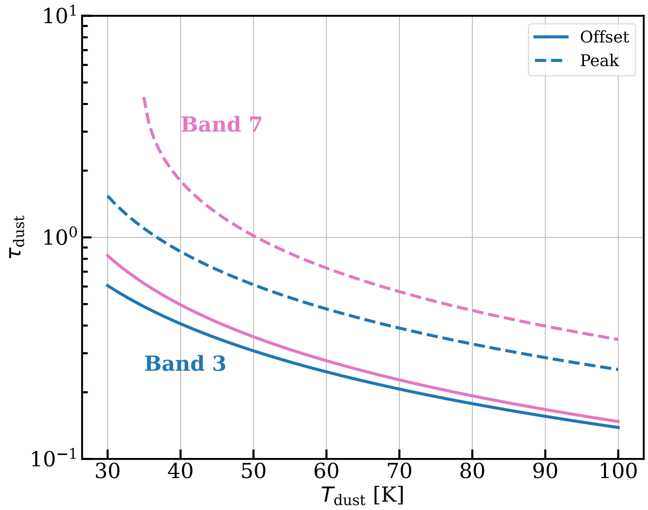

Fig. 4: Continuum optical depth as a function of temperature at the peak of the continuum (dashed) and the 0.5″ offset position where the spectrum was extracted (solid line). Blue shows the optical depth for the Band 3 continuum at a frequency of ∼91 GHz and pink shows the PILS continuum at a frequency of ∼348.815 GHz.

found F_ν to be within the beam of those observations at the peak of the continuum and at the ∼0.5″ offset position where the spectrum was extracted. For this measurement we used CASA (McMullin et al. 2007) version 6.5.2.26 and found the continuum flux density to be ∼1.16 Jy beam^{-1} and ∼0.55 Jy beam^{-1} at the peak and the offset position. We did the same for the Band 3 data at a frequency of ∼91 GHz and found the Band 3 continuum flux density to be $\sim 9.07\times10^{-2}$ Jy beam^{-1} and $\sim 5.25\times10^{-2}$ Jy beam^{-1} at the peak and the offset positions, respectively. Next, we calculated $\tau_{\rm dust}$ for a range of dust temperatures that are feasible for IRAS16293B as suggested by Jacobsen et al. (2018).

Figure 4 presents the continuum optical depth for the various temperatures. The temperature of the inner regions based on models of Jacobsen et al. (2018) is ∼90 K. At 90 K, both the PILS and Band 3 peak continuum are marginally optically thick with the PILS continuum having an optical depth of ∼1.5 times larger. However, at the location off-source, the dust optical depth for the PILS continuum is almost the same as that of Band 3, which is ∼0.15. Therefore, it is safe to assume that the dust at the offset location at $T_{\rm dust}$ = 90 K is almost completely optically thin in Band 3 and Band 7 datasets. Even assuming the unrealistic worst case scenario of $T_{\rm dust}$ = 30 K in Fig. 4 and assuming that all the dust is in a column between the observer and the protostar, the difference between Band 3 and Band 7 dust attenuation (i.e., $e^{-\tau}$) is around 25% at the offset location at most.

4.2. Comparison with PILS

In this section we compare the excitation temperatures and column densities of the same molecules detected in the PILS Band 7 survey and this work.

4.2.1. Excitation temperature

The measured excitation temperatures are presented in Fig. B.4. The species are roughly ordered by increasing binding energy (a measure of how strongly bound a molecule is in ices) from left to right. However, given that the uncertainties are relatively large, the number of detected lines for each species is small, and the lines are biased toward lower $E_{\rm up}$; it is not possible to identify a clear trend between the binding energies (or sublimation temperatures) and excitation temperatures. Another effect that can complicate the picture and change Fig. B.4 is that the molecules with lower binding energies than water are expected to desorb with water if initially mixed with it (Collings et al. 2004; Busch et al. 2022; Garrod et al. 2022). This would be in line with the measured excitation temperatures of the molecules toward the left hand side of Fig. B.4 being at around ∼100 K (i.e., the desorption temperature of water). Therefore, a strong trend might not be expected in Fig. B.4.

Nevertheless, our excitation temperatures mostly agree with those found by Jørgensen et al. (2018) for IRAS16293 B. The only exceptions are CH_3OCHO and CH_3CH_2OH where their excitation temperatures are found to be higher in PILS. This could be due to the lines that are covered in the Band 3 data having a lower $E_{\rm up}$ than those covered in the Band 7 data. For example, if the two lines of CH_3CH_2OH with $E_{\rm up}$∼80 − 90 K are ignored, a fit at $T_{\rm ex}$∼240 K (i.e., agreeing with the PILS temperature) can match the brightness temperatures of the rest of the lines within ∼40 − 50%. Our excitation temperatures also agree well with what is found for the companion source, IRAS16293A, in PILS (Manigand et al. 2020).

4.2.2. Column density

Making a direct comparison of the column densities from PILS and this work should be done with caution due to the different beam sizes in the two sets of observations. Therefore, before comparison, column densities of Band 7 were corrected to match the Band 3 results. PILS studies use a source size of 0.5″ in their analysis, while we found the column densities averaged over the Band 3 beam. Our assumption corresponds to the Band 3 emission filling the beam uniformly (i.e., $\theta_{\rm s} >> \theta_{\rm b}$). The PILS column densities were converted to an average over the PILS beam (or filling the PILS beam uniformly) by multiplication with their beam dilution factor of $\frac{0.5^2}{0.5^2+0.5^2} = 0.5$. After this modification, we also investigated how the different beam sizes in PILS and our study can affect the comparison (assuming that the column densities are averaged over the respective beams). Figure B.5 presents a two-dimensional Gaussian distribution with two circular regions representing the beams of Band 3 and Band 7. Assuming a uniform beam, we calculated the mean in the two beams and found around a 10% difference between these two, which is smaller than the typical uncertainties on the column densities and it was thus ignored.

Figure 5 presents the column densities from PILS and this work after correction for beam dilution. The column densities of PILS are taken from Coutens et al. (2016) (NH_2CHO), Jørgensen et al. (2016) (CH_2OHCHO, CHDOHCHO, gGg-$(CH_2OH)_2$, and CH_3COOH), Calcutt et al. (2018b) (CH_3CH_2CN, HC_3N), Jørgensen et al. (2018) (CH_3OH, $^{13}CH_3CHO$, CH_3CDO, CH_3CHO, CH_2DOH, CH_3CH_2OH, a-CH_3CHDOH, CH_3OCH_3, CH_3OCHO, a-a-CH_2DCH_2OH, and t-HCOOH), Persson et al. (2018) (D_2CO), Manigand et al. (2020) (CH_2DCHO), Drozdovskaya et al. (2022) (CHD_2OH), Ilyushin et al. (2022) (CD_3OH), Drozdovskaya et al. (2018) (CH_3SH), Ferrer Asensio et al. (2023) (CHD_2CHO), and Lykke et al. (2017) (CH_3COCH_3). In addition, we did not include $^{13}CH_2OHCHO$ and gGg-$(CH_2OH)_2$ in Fig. 5 because our measured column

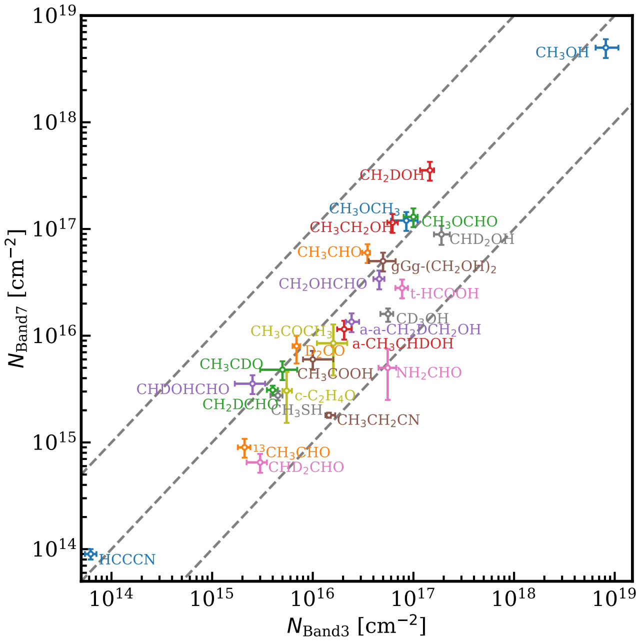

Fig. 5: Column density of the various molecules from the ALMA Band 7 observations (PILS; ∼345 GHz) as a function of those from Band 3 (∼100 GHz). Beam dilution was corrected for the column densities in this figure. Dashed lines present where the values of the y-axis are the same as the values of the x-axis, where they are ten times higher and ten times lower than the values of the x-axis.

densities are approximate. Moreover, the column density of CH_3COOH in PILS was found from old spectroscopic data (Jørgensen et al. 2016). To avoid a bias, we redid the fit to CH_3COOH in the Band 7 data using new spectroscopic data (Ilyushin et al. 2013; see Appendix A), and found that the column density in Jørgensen et al. (2016) was underestimated by a factor of about two. Therefore, in this work we refer to the updated column density of CH_3COOH using the new spectroscopic data (∼1.2×10^{16}).

Figure 5 shows that the column densities from the Band 3 observations generally agree with those of PILS. There are a few data points where the Band 3 column densities are ≳3 times higher than those of Band 7. Among those molecules, NH_2CHO and CH_3CH_2CN seem to be outliers that have Band 3 column densities that are ten times higher than Band 7. However, because the column densities of these two molecules in this work were measured based on only one line, those values should be considered with caution. Therefore, we excluded these two molecules from further analysis.

Taking only the molecules with at least three detected lines in Band 3 (see Table 1), the average of ($\log_{10}$ of) the Band 3 column densities weighted by the uncertainty on each data point is 4.4×10^{16} cm^{-2}. This value for Band 7 column densities (measured using many more lines per molecule due to the larger frequency coverage) is 2.7×10^{16} cm^{-2}. These two agree well within the uncertainties. Moreover, the scatter around the line of $N_{\rm Band3} = N_{\rm Band7}$ is a factor of 1.9 below the line and 1.8 above the line. Therefore, it can be concluded that there is a tight, one-to-one correlation between the two column densities with a scatter of less than a factor of two. This agrees well with the low dust optical depth found for the Band 3 and Band 7 observations at the offset location where the spectra were extracted.

4.2.3. Ratios

The column density ratios are normally more informative than absolute column densities because the latter depends on the beam and the assumed beam dilution factor. The left panel of Fig. 2 shows that the ratios with respect to methanol from Band 3 agree well with those from Band 7 (PILS) for almost all molecules. Figure 6 presents the ratio between the Band 3 and Band 7 results for individual molecules. This figure shows, even more clearly, that the results from the Band 3 data (this work) generally agree within a factor of about two with the results from the Band 7 data. Four molecules show larger than a factor of two difference between the two datasets and they are marked with an ellipse. This could be due to the lines of these species becoming optically thick. This argument is more convincing for CH_3CHO and CH_3CH_2OH given that there is good agreement between Band 3 and Band 7 results for their minor isotopologues. Moreover, the value for CH_2DOH is likely uncertain given that no single temperature could be fitted to its lines and hence the assumed T_{ex} does not fit all its lines equally well in this work (see Sect. 2.2). The slight variations between the Band 3 and Band 7 ratios could be due to the smaller number of lines covered in the Band 3 dataset compared with the PILS dataset, which also sets looser constraints on the excitation temperatures. Another factor in these variations could be the different beam sizes in the two datasets (see Sect. 4.2.2).

We found a good match between Band 3 and Band 7 data when comparing the ratios of the various COMs relative to methanol. The molecules that have column densities with a factor of > 2 difference between Band 3 and Band 7 in Fig. 5 (i.e., t-HCOOH, CD_3OH, and CHD_2CHO) show good agreement (factor of < 2) when their column density ratios with respect to methanol are compared between the two sets of observations.

4.3. *Comparison with other studies*

In this section we put some of the measured ratios (Fig. 2) in the context of other works. We mainly focus on the upper limit ratios because similar comparisons have been made in the PILS papers between the measured column density ratios of IRAS 16293 B and other sources. The ratios of aGg′- and gGg′-$(CH_2OH)_2$ to CH_3OH from our observations is between $\sim 4 \times 10^{-3}$ and $\sim 2 \times 10^{-2}$. The laboratory experiments and Monte Carlo simulations found the $(CH_2OH)_2/CH_3OH$ ratio to be $\sim 10^{-2} - 9 \times 10^{-2}$ and $\sim 2 \times 10^{-2} - 4 \times 10^{-2}$ (Fedoseev et al. 2015), which agrees with our observations. Moreover, Fedoseev et al. (2017) found a ratio of glycerol/ethylene glycol upper limit of around 0.01 in laboratory experiments which, from the ethylene glycol/methanol ratio of Fedoseev et al. (2015), gives a glycerol/methanol upper limit of between 10^{-4} and 9×10^{-4}. Our upper limit ratios of GGag′g′- and G′Gg′gg′-glycerol to methanol are $<10^{-4}$ and $<8 \times 10^{-4}$, which are on the same order of magnitude as reported in laboratory experiments and Monte Carlo simulations (Fedoseev et al. 2015, 2017).

Propanal was found to form n-propanol (Qasim et al. 2019a,b), and both were not detected in the Band 3 data. However, we note that propanal was detected toward IRAS 16293 B by PILS (Lykke et al. 2017) and Qasim et al. (2019a) found that the ratio of their upper limit ratio for n-propanol/propanal for IRAS 16293 B is consistent with their laboratory experiments.

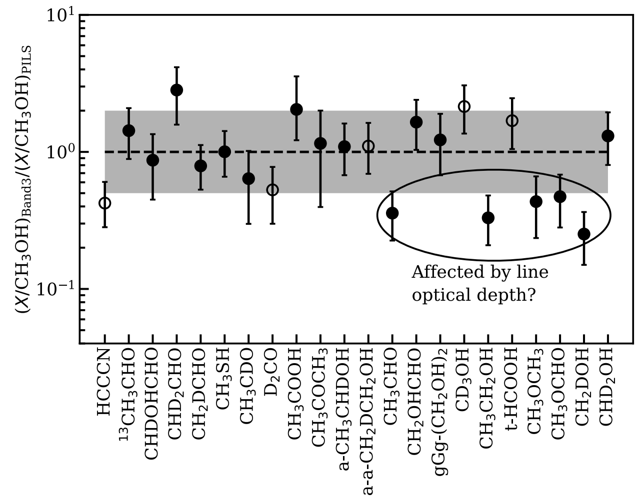

Fig. 6: Ratio between Band 3 and PILS column density ratios with respect to methanol (i.e., the ratio of blue to pink from the left panel of Fig. 2). The horizontal dashed line indicates where the ratio between Band 3 and PILS are the same. The shaded gray area indicates the region with a factor of two difference between Band 3 and PILS results. The species are ordered in the same way as in the left panel of Fig. 2. The hollow symbols show the species that have only one detected line.

Our upper limit ratio of Ga-n-propanol/methanol is $<7 \times 10^{-4}$, which is a factor of about six lower than the detected ratio toward G+0.693-0.027 ($\sim 4 \times 10^{-3}$; Jiménez-Serra et al. 2022 and methanol from Rodríguez-Almeida et al. 2021). Our upper limit ratios of g-, a-Isopropanol, and Ga-n-propanol with respect to methanol agree within a factor of about two with those detected toward Sgr B2(N2b) (~0.002; Belloche et al. 2022). Band 3 ratios of s- and g-propanal/methanol are $<2 \times 10^{-4}$ and <0.04, respectively. These are in agreement with the abundance ratios of propanal/methanol in TMC-1 (around 0.01, Agúndez et al. 2023) and PILS (around 2×10^{-4}; Lykke et al. 2017). Moreover, the abundance of indene with respect to H_2 toward TMC-1 (Cernicharo et al. 2021) is on the same order of magnitude as our upper limit ratio of indene/H_2, assuming a lower limit on the H_2 column density of 10^{25} cm^{-2} from Jørgensen et al. (2016) for IRAS 16293 B. However, using the same lower limit column density for H_2 toward IRAS 16293 B, our upper limit abundances of 1-CNN, 2-CNN, and benzonitrile are a factor of about two to ten lower than what is found for TMC-1 (Gratier et al. 2016; McGuire et al. 2021).

The Band 3 upper limit ratio of urea/methanol is $<2 \times 10^{-5}$, which is in-line and on the lower end of the observed range (either upper limit or detected) in the literature toward SgrB2 (Belloche et al. 2019), NGC 6334I (Ligterink et al. 2020), and G+0.693-0.027 systems (Zeng et al. 2023). The upper limit $NH^{13}CHO/CH_3OH$ in this work is consistent with the detected ratios toward NGC 6334I (Ligterink et al. 2020; methanol from Bøgelund et al. 2018) and G+0.693-0.027 systems (Zeng et al. 2023; methanol from Rodríguez-Almeida et al. 2021). Moreover, the upper limit ratios of z-cyanomethanimine and glyceraldehyde to methanol toward G+0.693-0.027 (Jiménez-Serra et al. 2020) are consistent with our upper limit ratios. However, the ratio of ethanolamine/methanol toward this source (Rivilla et al. 2021) was found to be around one order of magnitude higher than the Band 3 upper limit measurement of IRAS 16293

B. The discussed ratios in this section may be generally higher in G+0.693-0.027 than IRAS 16293 B. Given the small sample size and the upper limit nature of our results, it is not possible to draw further conclusions on the significance of these differences and similarities. This is particularly the case, because of the upper limits reported here tend to depend on the assumed excitation temperature and more importantly the lines covered in our data.

5. Conclusions

We analyzed the deep ALMA Band 3 (~100 GHz) data of IRAS16293 B in this work. We searched for large organic species in this dataset and derived the corresponding column densities and excitation temperatures of various oxygen-, nitrogen-, and sulfur-bearing molecules. Below are the main conclusions of this work.

- The line density for lines detected at a $\gtrsim 6\sigma$ level in Band 3 observations is one per ~8.5 MHz, which is only ~2.5 times lower than that of PILS: the spectrum is relatively rich and crowded even at ~3 mm observations.
- We detected around 31 molecules (including minor isotopologues), thereof ~15 tentatively, in the Band 3 dataset. These include O-bearing COMs such as CH_3OH, CH_2OHCHO, CH_3OCH_3, CH_3OCHO, gGg-$(CH_2OH)_2$, CH_3COCH_3, and c-C_2H_4O. We also tentatively detected a few N- and S-bearing species such as $HOCH_2CN$ and CH_3SH.
- We searched for many large COMs among which are glycerol and isopropanol, but we did not detect them. The upper limits on the 41 non-detected species are also provided, which generally agree with the previous laboratory experiments and observations.
- In the Band 3 spectrum, ~25 – 30% of all lines at the $\gtrsim 6\sigma$ level were not identified. This points to the need for additional spectroscopic information.
- We find good agreement between the column densities of Band 3 and Band 7 observations with a scatter of less than a factor of two. Moreover, the Band 3 ratios with respect to methanol agree within a factor of about two with those from the Band 7 observations.
- We conclude that around IRAS16293 B, the dust optical depth does not affect the column densities and the ratios of various molecules, especially for the spectrum extracted from a position off-source (where the dust column density is lower than on-source).

Acknowledgements. We thank the referee for the helpful and constructive comments. We thank A. Hacar for his invaluable help with the data reduction. Astrochemistry in Leiden is supported by the Netherlands Research School for Astronomy (NOVA), by funding from the European Research Council (ERC) under the European Union's Horizon 2020 research and innovation programme (grant agreement No. 101019751 MOLDISK), and by the Dutch Research Council (NWO) grant 618.000.001. Support by the Danish National Research Foundation through the Center of Excellence "InterCat" (Grant agreement no.: DNRF150) is also acknowledged. J.K.J. acknowledges support from the Independent Research Fund Denmark (grant number 0135-00123B). M.N.D. acknowledges the Swiss National Science Foundation (SNSF) Ambizione grant number 180079, the Center for Space and Habitability (CSH) Fellowship, and the IAU Gruber Foundation Fellowship. G.F. acknowledges the financial support from the European Union's Horizon 2020 research and innovation program under the Marie Sklodowska-Curie grant agreement No. 664931. R.T.G. acknowledges funding from the National Science Foundation Astronomy & Astrophysics program (grant number 2206516). H.S.P.M. acknowledges support by the Deutsche Forschungsgemeinschaft (DFG) via the collaborative research grant SFB 956 (project ID 184018867). S.F.W. acknowledges the financial support of the SNSF Eccellenza Professorial Fellowship (PCEFP2_181150). This paper makes use of the following ALMA data: ADS/JAO.ALMA#2017.1.00518.S and #2013.1.00278.S. ALMA is a partnership of ESO (representing its member states), NSF (USA) and NINS (Japan), together with NRC (Canada), MOST and ASIAA (Taiwan), and KASI (Republic of Korea), in cooperation with the Republic of Chile. The Joint ALMA Observatory is operated by ESO, AUI/NRAO and NAOJ. The National Radio Astronomy Observatory is a facility of the National Science Foundation operated under cooperative agreement by Associated Universities, Inc.

References

Agúndez, M., Loison, J. C., Hickson, K. M., et al. 2023, A&A, 673, A34
Bacmann, A., Faure, A., & Berteaud, J. 2019, ACS Earth and Space Chemistry, 3, 1000
Bacmann, A., Taquet, V., Faure, A., Kahane, C., & Ceccarelli, C. 2012, A&A, 541, L12
Barone, V., Latouche, C., Skouteris, D., et al. 2015, MNRAS, 453, L31
Baskakov, O. I., Alekseev, E. A., Motiyenko, R. A., et al. 2006, Journal of Molecular Spectroscopy, 240, 188
Belloche, A., Garrod, R. T., Müller, H. S. P., et al. 2019, A&A, 628, A10
Belloche, A., Garrod, R. T., Zingsheim, O., Müller, H. S. P., & Menten, K. M. 2022, A&A, 662, A110
Belloche, A., Maury, A. J., Maret, S., et al. 2020, A&A, 635, A198
Belloche, A., Müller, H. S. P., Menten, K. M., Schilke, P., & Comito, C. 2013, A&A, 559, A47
Bergner, J. B., Öberg, K. I., Garrod, R. T., & Graninger, D. M. 2017, ApJ, 841, 120
Bianchi, E., López-Sepulcre, A., Ceccarelli, C., et al. 2022, ApJ, 928, L3
Bisschop, S. E., Jørgensen, J. K., Bourke, T. L., Bottinelli, S., & van Dishoeck, E. F. 2008, A&A, 488, 959
Blake, G. A., Sutton, E. C., Masson, C. R., & Phillips, T. G. 1987, ApJ, 315, 621
Bocquet, R., Demaison, J., Cosléou, J., et al. 1999, Journal of Molecular Spectroscopy, 195, 345
Bøgelund, E. G., McGuire, B. A., Ligterink, N. F. W., et al. 2018, A&A, 615, A88
Booth, A. S., Walsh, C., Terwisscha van Scheltinga, J., et al. 2021, Nature Astronomy, 5, 684
Bouchez, A., Margulès, L., Motiyenko, R. A., et al. 2012, A&A, 540, A51
Brauer, C. S., Pearson, J. C., Drouin, B. J., & Yu, S. 2009, ApJS, 184, 133
Brunken, N. G. C., Booth, A. S., Leemker, M., et al. 2022, A&A, 659, A29
Busch, L. A., Belloche, A., Garrod, R. T., Müller, H. S. P., & Menten, K. M. 2022, A&A, 665, A96
Butner, H. M., Charnley, S. B., Ceccarelli, C., et al. 2007, ApJ, 659, L137
Calcutt, H., Fiechter, M. R., Willis, E. R., et al. 2018a, A&A, 617, A95
Calcutt, H., Jørgensen, J. K., Müller, H. S. P., et al. 2018b, A&A, 616, A90
Cazaux, S., Tielens, A. G. G. M., Ceccarelli, C., et al. 2003, ApJ, 593, L51
Ceccarelli, C., Bacmann, A., Boogert, A., et al. 2010, A&A, 521, L22
Ceccarelli, C., Codella, C., Balucani, N., et al. 2022, arXiv e-prints, arXiv:2206.13270
Cernicharo, J., Agúndez, M., Cabezas, C., et al. 2021, A&A, 649, L15
Chen, Y., van Gelder, M. L., Nazari, P., et al. 2023, arXiv e-prints, arXiv:2308.02688
Christen, D., Coudert, L. H., Larsson, J. A., & Cremer, D. 2001, Journal of Molecular Spectroscopy, 205, 185
Christen, D., Coudert, L. H., Suenram, R. D., & Lovas, F. J. 1995, Journal of Molecular Spectroscopy, 172, 57
Christen, D. & Müller, H. S. P. 2003, Physical Chemistry Chemical Physics (Incorporating Faraday Transactions), 5, 3600
Chuang, K. J., Fedoseev, G., Qasim, D., et al. 2020, A&A, 635, A199
Chuang, K. J., Fedoseev, G., Scirè, C., et al. 2021, A&A, 650, A85
Chuang, K. J., Jäger, C., Krasnokutski, S. A., Fulvio, D., & Henning, T. 2022, ApJ, 933, 107
Coletta, A., Fontani, F., Rivilla, V. M., et al. 2020, A&A, 641, A54
Collings, M. P., Anderson, M. A., Chen, R., et al. 2004, MNRAS, 354, 1133
Coudert, L. H., Margulès, L., Vastel, C., et al. 2019, A&A, 624, A70
Coutens, A., Jørgensen, J. K., van der Wiel, M. H. D., et al. 2016, A&A, 590, L6
Coutens, A., Loison, J. C., Boulanger, A., et al. 2022, A&A, 660, L6
Creswell, R. A. & Schwendeman, R. H. 1974, Chemical Physics Letters, 27, 521
Creswell, R. A., Winnewisser, G., & Gerry, M. C. L. 1977, Journal of Molecular Spectroscopy, 65, 420
Dangoisse, D., Willemot, E., & Bellet, J. 1978, Journal of Molecular Spectroscopy, 71, 414
De Simone, M., Ceccarelli, C., Codella, C., et al. 2020, ApJ, 896, L3
de Zafra, R. L. 1971, Astrophysical Journal, vol. 170, p. 165, 170, 165
Dickens, J. E., Irvine, W. M., Ohishi, M., et al. 1997, ApJ, 489, 753
Drozdovskaya, M. N., Coudert, L. H., Margulès, L., et al. 2022, A&A, 659, A69
Drozdovskaya, M. N., van Dishoeck, E. F., Jørgensen, J. K., et al. 2018, MNRAS, 476, 4949
Drozdovskaya, M. N., van Dishoeck, E. F., Rubin, M., Jørgensen, J. K., & Altwegg, K. 2019, MNRAS, 490, 50

Durig, J. R., Bucy, W. E., Wurrey, C. J., & Carreira, L. A. 1975, The Journal of Physical Chemistry, 79, 988
Endres, C. P., Drouin, B. J., Pearson, J. C., et al. 2009, A&A, 504, 635
Fedoseev, G., Chuang, K. J., Ioppolo, S., et al. 2017, ApJ, 842, 52
Fedoseev, G., Cuppen, H. M., Ioppolo, S., Lamberts, T., & Linnartz, H. 2015, MNRAS, 448, 1288
Fedoseev, G., Qasim, D., Chuang, K.-J., et al. 2022, ApJ, 924, 110
Ferrer Asensio, J., Spezzano, S., Coudert, L. H., et al. 2023, A&A, 670, A177
Fukuyama, Y., Odashima, H., Takagi, K., & Tsunekawa, S. 1996, ApJS, 104, 329
Garrod, R. T., Jin, M., Matis, K. A., et al. 2022, ApJS, 259, 1
Gratier, P., Majumdar, L., Ohishi, M., et al. 2016, ApJS, 225, 25
Groner, P., Albert, S., Herbst, E., et al. 2002, ApJS, 142, 145
Haykal, I., Motiyenko, R. A., Margulès, L., & Huet, T. R. 2013, A&A, 549, A96
Herbst, E. & van Dishoeck, E. F. 2009, ARA&A, 47, 427
Hirose, C. 1974, ApJ, 189, L145
Hirota, E., Sugisaki, R., Nielsen, C. J., & Sørensen, G. O. 1974, Journal of Molecular Spectroscopy, 49, 251
Hsu, S.-Y., Liu, S.-Y., Liu, T., et al. 2022, ApJ, 927, 218
Ikeda, M., Ohishi, M., Nummelin, A., et al. 2001, ApJ, 560, 792
Ilyushin, V., Kryvda, A., & Alekseev, E. 2009, Journal of Molecular Spectroscopy, 255, 32
Ilyushin, V. V., Endres, C. P., Lewen, F., Schlemmer, S., & Drouin, B. J. 2013, Journal of Molecular Spectroscopy, 290, 31
Ilyushin, V. V., Müller, H. S. P., Jørgensen, J. K., et al. 2022, A&A, 658, A127
Ioppolo, S., Fedoseev, G., Chuang, K. J., et al. 2021, Nature Astronomy, 5, 197
Jaber, A. A., Ceccarelli, C., Kahane, C., & Caux, E. 2014, ApJ, 791, 29
Jacobsen, S. K., Jørgensen, J. K., van der Wiel, M. H. D., et al. 2018, A&A, 612, A72
Jiménez-Serra, I., Martín-Pintado, J., Rivilla, V. M., et al. 2020, Astrobiology, 20, 1048
Jiménez-Serra, I., Rodríguez-Almeida, L. F., Martín-Pintado, J., et al. 2022, A&A, 663, A181
Jiménez-Serra, I., Vasyunin, A. I., Caselli, P., et al. 2016, ApJ, 830, L6
Jones, B. M., Bennett, C. J., & Kaiser, R. I. 2011, ApJ, 734, 78
Jørgensen, J. K., Belloche, A., & Garrod, R. T. 2020, ARA&A, 58, 727
Jørgensen, J. K., Bourke, T. L., Nguyen Luong, Q., & Takakuwa, S. 2011, A&A, 534, A100
Jørgensen, J. K., Favre, C., Bisschop, S. E., et al. 2012, ApJ, 757, L4
Jørgensen, J. K., Müller, H. S. P., Calcutt, H., et al. 2018, A&A, 620, A170
Jørgensen, J. K., Schöier, F. L., & van Dishoeck, E. F. 2002, A&A, 389, 908
Jørgensen, J. K., van der Wiel, M. H. D., Coutens, A., et al. 2016, A&A, 595, A117
Kahane, C., Ceccarelli, C., Faure, A., & Caux, E. 2013, ApJ, 763, L38
Kleiner, I., Lovas, F. J., & Godefroid, M. 1996, Journal of Physical and Chemical Reference Data, 25, 1113
Kryvda, A. V., Gerasimov, V. G., Dyubko, S. F., Alekseev, E. A., & Motiyenko, R. A. 2009, Journal of Molecular Spectroscopy, 254, 28
Kukolich, S. G. & Nelson, A. C. 1971, Chemical Physics Letters, 11, 383
Lauvergnat, D., Coudert, L. H., Klee, S., & Smirnov, M. 2009, Journal of Molecular Spectroscopy, 256, 204
Ligterink, N. F. W., Ahmadi, A., Coutens, A., et al. 2021, A&A, 647, A87
Ligterink, N. F. W., El-Abd, S. J., Brogan, C. L., et al. 2020, ApJ, 901, 37
Ligterink, N. F. W. & Minissale, M. 2023, arXiv e-prints, arXiv:2306.09071
López-Sepulcre, A., Sakai, N., Neri, R., et al. 2017, A&A, 606, A121
Lykke, J. M., Coutens, A., Jørgensen, J. K., et al. 2017, A&A, 597, A53
Mallinson, P. & Fayt, A. 1976, Molecular Physics, 32, 473
Manigand, S., Calcutt, H., Jørgensen, J. K., et al. 2019, A&A, 623, A69
Manigand, S., Coutens, A., Loison, J. C., et al. 2021, A&A, 645, A53
Manigand, S., Jørgensen, J. K., Calcutt, H., et al. 2020, A&A, 635, A48
Margulès, L., Coutens, A., Ligterink, N. F. W., et al. 2023, MNRAS, 524, 1211
Margulès, L., McGuire, B. A., Senent, M. L., et al. 2017, A&A, 601, A50
Margulès, L., Motiyenko, R. A., Ilyushin, V. V., & Guillemin, J. C. 2015, A&A, 579, A46
Maureira, M. J., Pineda, J. E., Segura-Cox, D. M., et al. 2020, ApJ, 897, 59
McClure, M. K., Rocha, W. R. M., Pontoppidan, K. M., et al. 2023, Nature Astronomy, 7, 431
McGuire, B. A. 2022, ApJS, 259, 30
McGuire, B. A., Burkhardt, A. M., Loomis, R. A., et al. 2020, ApJ, 900, L10
McGuire, B. A., Loomis, R. A., Burkhardt, A. M., et al. 2021, Science, 371, 1265
McMullin, J. P., Waters, B., Schiebel, D., Young, W., & Golap, K. 2007, in Astronomical Society of the Pacific Conference Series, Vol. 376, Astronomical Data Analysis Software and Systems XVI, ed. R. A. Shaw, F. Hill, & D. J. Bell, 127
McNaughton, D., Jahn, M. K., Travers, M. J., et al. 2018, MNRAS, 476, 5268
Medcraft, C., Thompson, C. D., Robertson, E. G., Appadoo, D. R. T., & McNaughton, D. 2012, ApJ, 753, 18
Milam, S. N., Savage, C., Brewster, M. A., Ziurys, L. M., & Wyckoff, S. 2005, ApJ, 634, 1126
Minissale, M., Aikawa, Y., Bergin, E., et al. 2022, ACS Earth and Space Chemistry, 6, 597
Motiyenko, R. A., Tercero, B., Cernicharo, J., & Margulès, L. 2012, A&A, 548, A71
Müller, H. S. P., Belloche, A., Xu, L.-H., et al. 2016, A&A, 587, A92
Müller, H. S. P. & Christen, D. 2004, Journal of Molecular Spectroscopy, 228, 298
Müller, H. S. P., Jørgensen, J. K., Guillemin, J.-C., Lewen, F., & Schlemmer, S. 2023a, MNRAS, 518, 185
Müller, H. S. P., Jørgensen, J. K., Guillemin, J.-C., Lewen, F., & Schlemmer, S. 2023b, Journal of Molecular Spectroscopy, 394, 111777
Müller, H. S. P., Schlöder, F., Stutzki, J., & Winnewisser, G. 2005, Journal of Molecular Structure, 742, 215
Müller, H. S. P., Thorwirth, S., Roth, D. A., & Winnewisser, G. 2001, A&A, 370, L49
Murillo, N. M., Hsieh, T. H., & Walsh, C. 2022a, A&A, 665, A68
Murillo, N. M., van Dishoeck, E. F., Hacar, A., Harsono, D., & Jørgensen, J. K. 2022b, A&A, 658, A53
Nazari, P., Meijerhof, J. D., van Gelder, M. L., et al. 2022a, A&A, 668, A109
Nazari, P., Tabone, B., & Rosotti, G. P. 2023a, A&A, 671, A107
Nazari, P., Tabone, B., Rosotti, G. P., & van Dishoeck, E. F. 2023b, Submitted to A&A
Nazari, P., Tabone, B., Rosotti, G. P., et al. 2022b, A&A, 663, A58
Nazari, P., Tabone, B., van 't Hoff, M. L. R., Jørgensen, J. K., & van Dishoeck, E. F. 2023c, arXiv e-prints, arXiv:2306.11778
Nazari, P., van Gelder, M. L., van Dishoeck, E. F., et al. 2021, A&A, 650, A150
Nummelin, A., Dickens, J. E., Bergman, P., et al. 1998, A&A, 337, 275
Öberg, K. I., Boogert, A. C. A., Pontoppidan, K. M., et al. 2011, ApJ, 740, 109
Öberg, K. I., Garrod, R. T., van Dishoeck, E. F., & Linnartz, H. 2009, A&A, 504, 891
Öberg, K. I., Guzmán, V. V., Furuya, K., et al. 2015, Nature, 520, 198
Ordu, M. H., Zingsheim, O., Belloche, A., et al. 2019, A&A, 629, A72
Pearson, J. C., Brauer, C. S., & Drouin, B. J. 2008, Journal of Molecular Spectroscopy, 251, 394
Pearson, J. C., Sastry, K. V. L. N., Herbst, E., & De Lucia, F. C. 1994, ApJS, 93, 589
Pearson, J. C., Yu, S., & Drouin, B. J. 2012, Journal of Molecular Spectroscopy, 280, 119
Perrin, A., Flaud, J. M., Bakri, B., et al. 2002, Journal of Molecular Spectroscopy, 216, 203
Persson, M. V., Harsono, D., Tobin, J. J., et al. 2016, A&A, 590, A33
Persson, M. V., Jørgensen, J. K., Müller, H. S. P., et al. 2018, A&A, 610, A54
Pickett, H. M., Poynter, R. L., Cohen, E. A., et al. 1998, J. Quant. Spectr. Rad. Transf., 60, 883
Qasim, D., Fedoseev, G., Chuang, K. J., et al. 2019a, A&A, 627, A1
Qasim, D., Fedoseev, G., Lamberts, T., et al. 2019b, ACS Earth and Space Chemistry, 3, 986
Requena-Torres, M. A., Martín-Pintado, J., Martín, S., & Morris, M. R. 2008, ApJ, 672, 352
Requena-Torres, M. A., Martín-Pintado, J., Rodríguez-Franco, A., et al. 2006, A&A, 455, 971
Rivilla, V. M., Beltrán, M. T., Cesaroni, R., et al. 2017, A&A, 598, A59
Rivilla, V. M., Jiménez-Serra, I., Martín-Pintado, J., et al. 2021, Proceedings of the National Academy of Science, 118, e2101314118
Rivilla, V. M., Jiménez-Serra, I., Martín-Pintado, J., et al. 2022, Frontiers in Astronomy and Space Sciences, 9, 876870
Rocha, W. R. M., Rachid, M. G., Olsthoorn, B., et al. 2022, A&A, 668, A63
Rodríguez-Almeida, L. F., Jiménez-Serra, I., Rivilla, V. M., et al. 2021, ApJ, 912, L11
Sánchez-Monge, Á., Schilke, P., Ginsburg, A., Cesaroni, R., & Schmiedeke, A. 2018, A&A, 609, A101
Schutte, W. A., Boogert, A. C. A., Tielens, A. G. G. M., et al. 1999, A&A, 343, 966
Scibelli, S. & Shirley, Y. 2020, ApJ, 891, 73
Taniguchi, K., Sanhueza, P., Olguin, F. A., et al. 2023, ApJ, 950, 57
Taquet, V., van Dishoeck, E. F., Swayne, M., et al. 2018, A&A, 618, A11
Theulé, P., Duvernay, F., Danger, G., et al. 2013, Advances in Space Research, 52, 1567
Thorwirth, S., Müller, H. S. P., & Winnewisser, G. 2000, Journal of Molecular Spectroscopy, 204, 133
van Dishoeck, E. F., Blake, G. A., Jansen, D. J., & Groesbeck, T. D. 1995, ApJ, 447, 760
van Gelder, M. L., Jaspers, J., Nazari, P., et al. 2022a, A&A, 667, A136
van Gelder, M. L., Nazari, P., Tabone, B., et al. 2022b, A&A, 662, A67
van Gelder, M. L., Tabone, B., Tychoniec, Ł., et al. 2020, A&A, 639, A87
Vastel, C., Bottinelli, S., Caux, E., Glorian, J. M., & Boiziot, M. 2015, in SF2A-2015: Proceedings of the Annual meeting of the French Society of Astronomy and Astrophysics, 313–316
Vazart, F., Ceccarelli, C., Balucani, N., Bianchi, E., & Skouteris, D. 2020, MNRAS, 499, 5547
Walsh, C., Loomis, R. A., Öberg, K. I., et al. 2016, ApJ, 823, L10

Walters, A., Schäfer, M., Ordu, M. H., et al. 2015, Journal of Molecular Spectroscopy, 314, 6
Winnewisser, M., Winnewisser, B. P., Stein, M., et al. 2002, Journal of Molecular Spectroscopy, 216, 259
Wootten, A. 1989, ApJ, 337, 858
Xu, L.-H. & Lovas, F. J. 1997, Journal of Physical and Chemical Reference Data, 26, 17
Yamada, K. M. T., Moravec, A., & Winnewisser, G. 1995, Zeitschrift Naturforschung Teil A, 50, 1179
Yang, Y.-L., Green, J. D., Pontoppidan, K. M., et al. 2022, ApJ, 941, L13
Yang, Y.-L., Sakai, N., Zhang, Y., et al. 2021, ApJ, 910, 20
Zakharenko, O., Ilyushin, V. V., Lewen, F., et al. 2019, A&A, 629, A73
Zeng, S., Quénard, D., Jiménez-Serra, I., et al. 2019, MNRAS, 484, L43
Zeng, S., Rivilla, V. M., Jiménez-Serra, I., et al. 2023, MNRAS, 523, 1448

[1] Leiden Observatory, Leiden University, P.O. Box 9513, 2300 RA Leiden, the Netherlands
e-mail: nazari@strw.leidenuniv.nl
[2] Department of Chemistry, Massachusetts Institute of Technology, Cambridge, MA 02139, USA
[3] Max-Planck-Institut für extraterrestrische Physik, Giessenbachstr. 1, 85748 Garching, Germany
[4] Instituto de Astronomía, Universidad Nacional Autónoma de México, AP106, Ensenada CP 22830, B. C., México
[5] Star and Planet Formation Laboratory, RIKEN Cluster for Pioneering Research, Wako, Saitama 351-0198, Japan
[6] Niels Bohr Institute, University of Copenhagen, Øster Voldgade 5–7, 1350 Copenhagen K., Denmark
[7] SKA Organization, Jodrell Bank Observatory, Lower Withington, Macclesfield, Cheshire SK11 9FT, UK
[8] Laboratory for Astrophysics, Leiden Observatory, Leiden University, P.O. Box 9513, 2300 RA Leiden, the Netherlands
[9] Center for Space and Habitability, Universität Bern, Gesellschaftsstrasse 6, CH-3012 Bern, Switzerland
[10] INAF - Osservatorio Astrofisico di Catania, via Santa Sofia 78, 95123 Catania
[11] Departments of Astronomy and Chemistry, University of Virginia, Charlottesville, VA 22904, USA
[12] Center for Interstellar Catalysis, Department of Physics and Astronomy, Aarhus University, Ny Munkegade 120, Aarhus C 8000, Denmark
[13] National Radio Astronomy Observatory, Charlottesville, VA 22903, USA
[14] Astrophysik/I. Physikalisches Institut, Universität zu Köln, Zülpicher Str. 77, 50937 Köln, Germany
[15] Southwest Research Institute, San Antonio, TX 78238, USA

Table A.1: Spectroscopic information

Name	Species	Catalog	References
Methanol	$^{13}CH_3OH$	CDMS	Xu & Lovas (1997)
Methanol	CH_2DOH	JPL	Pearson et al. (2012)
Methanol	CHD_2OH	CDMS	Drozdovskaya et al. (2022)
Methanol	CD_3OH	CDMS	Ilyushin et al. (2022)
Acetaldehyde	CH_3CHO	JPL	Kleiner et al. (1996)
Acetaldehyde	$^{13}CH_3CHO$	CDMS	Margulès et al. (2015)
Acetaldehyde	CH_2DCHO	CDMS	Coudert et al. (2019)
Acetaldehyde	CH_3CDO	CDMS	Coudert et al. (2019)
Acetaldehyde	CHD_2CHO	JPL format	Ferrer Asensio et al. (2023)
Acetic acid	CH_3COOH	CDMS	Ilyushin et al. (2013)
Glycolaldehyde	CH_2OHCHO	CDMS	Müller 2021, unpublished
Glycolaldehyde	$^{13}CH_2OHCHO$	CDMS	Haykal et al. (2013)
Glycolaldehyde	CHDOHCHO	CDMS	Bouchez et al. (2012)
Ethanol	CH_3CH_2OH	CDMS	Pearson et al. (2008); Müller et al. (2016)
Ethanol	a-a-CH_2DCH_2OH	CDMS	Walters et al. (2015)
Ethanol	a-CH_3CHDOH	CDMS	Walters et al. (2015)
Dimethyl ether	CH_3OCH_3	CDMS	Endres et al. (2009)
Methyl formate	CH_3OCHO	JPL	Ilyushin et al. (2009)
aGg′-ethylene glycol	aGg′-$(CH_2OH)_2$	CDMS	Christen et al. (1995); Christen & Müller (2003)
gGg′-ethylene glycol	gGg′-$(CH_2OH)_2$	CDMS	Christen et al. (2001); Müller & Christen (2004)
Formaldehyde	D_2CO	CDMS	Dangoisse et al. (1978); Bocquet et al. (1999)
Cyanoacetylene	HCCCN	CDMS	de Zafra (1971); Creswell et al. (1977); Yamada et al. (1995); Thorwirth et al. (2000)
Ethyl cyanide	CH_3CH_2CN	CDMS	Pearson et al. 1994; Fukuyama et al. 1996; Brauer et al. 2009
Formamide	NH_2CHO	CDMS	Kukolich & Nelson 1971; Hirota et al. 1974; Kryvda et al. 2009; Motiyenko et al. 2012
Acetone	CH_3COCH_3	JPL	Groner et al. (2002); Ordu et al. (2019)
Formic acid	t-HCOOH	CDMS	Winnewisser et al. (2002)
Ethylene oxide	c-C_2H_4O	CDMS	Creswell & Schwendeman (1974); Hirose (1974); Medcraft et al. (2012)
Ethylene oxide	c-C_2H_3DO	CDMS	Müller et al. (2023a)
Methanethiol	CH_3SH	CDMS	Zakharenko et al. (2019)
Glycolonitrile	$HOCH_2CN$	CDMS	Margulès et al. (2017)

Notes. For acetone, we use a corrected entry (Ordu et al. 2019) for the apparent issues seen in Lykke et al. (2017).

Appendix A: Spectroscopic data

The spectroscopic information are summarized in Table A.1. The vibrational correction factor is assumed as one for all molecules except for the following species. The vibrational correction factor of 1.457 was used for CH_2DOH at a temperature of 300 K (Lauvergnat et al. 2009; Jørgensen et al. 2018). For CH_2OHCHO, a factor of 2.86 was adopted at 300K to take the higher (than ground state) vibrational states into account, which were calculated in the harmonic approximation. For $^{13}CH_2OHCHO$ and CHDOHCHO, a vibrational factor of 2.8 was used at a temperature of 300 K (Jørgensen et al. 2016). An upper limit vibrational factor of 2.824 at 300 K (Durig et al. 1975; Jørgensen et al. 2018) was assumed for a-a-CH_2DCH_2OH and a-CH_3CHDOH. Moreover, following Jørgensen et al. (2018), we multiplied the column densities of these two species by an additional factor of ∼2.69 to account for the presence of the gauche conformer. We assumed a vibration correction factor of 4.02 for aGg-$(CH_2OH)_2$ and gGg-$(CH_2OH)_2$ and added an additional factor of ∼1.38 to include the contribution from the higher gGg conformer at 300 K (Müller & Christen 2004; Jørgensen et al. 2016). A vibrational correction factor of 1.09 at 100 K was used for HCCCN (Mallinson & Fayt 1976; Calcutt et al. 2018b). For CH_3CH_2CN, a vibrational correction factor of 1.113 was assumed at 100 K. A vibrational correction factor of 1.5 was assumed for NH_2CHO at 300 K. For t-HCOOH, a vibrational correction factor of 1.103 at 300 K was assumed (Perrin et al. 2002; Baskakov et al. 2006; Jørgensen et al. 2018).

Appendix B: Additional plots and tables

Figure B.1 presents the fitted models of each molecule to the Band 3 data, highlighting a number of lines that are yet to be determined. Figures B.2 and B.3 present the transitions of Ga-n-propanol and G′Gg′gg′-Glycerol with the models determining their upper limits in orange. The total fit to the detected and tentative molecules is also shown in cyan. Figure B.4 presents the excitation temperatures when a measurement was possible for Band 3 results (PILS temperatures are shown for comparison). Figure B.5 shows the comparison of Band 3 and Band 7 beams on top of a two-dimensional Gaussian distribution, representing the spatial extents of COMs (e.g., see Jørgensen et al. 2016). This was done to examine the difference between the mean flux in the two beams, which is around 10%. Table B.1 shows the upper limits found for the molecules searched for but not detected. Table B.2 presents the covered transitions of the (tentatively) detected molecules in the data.

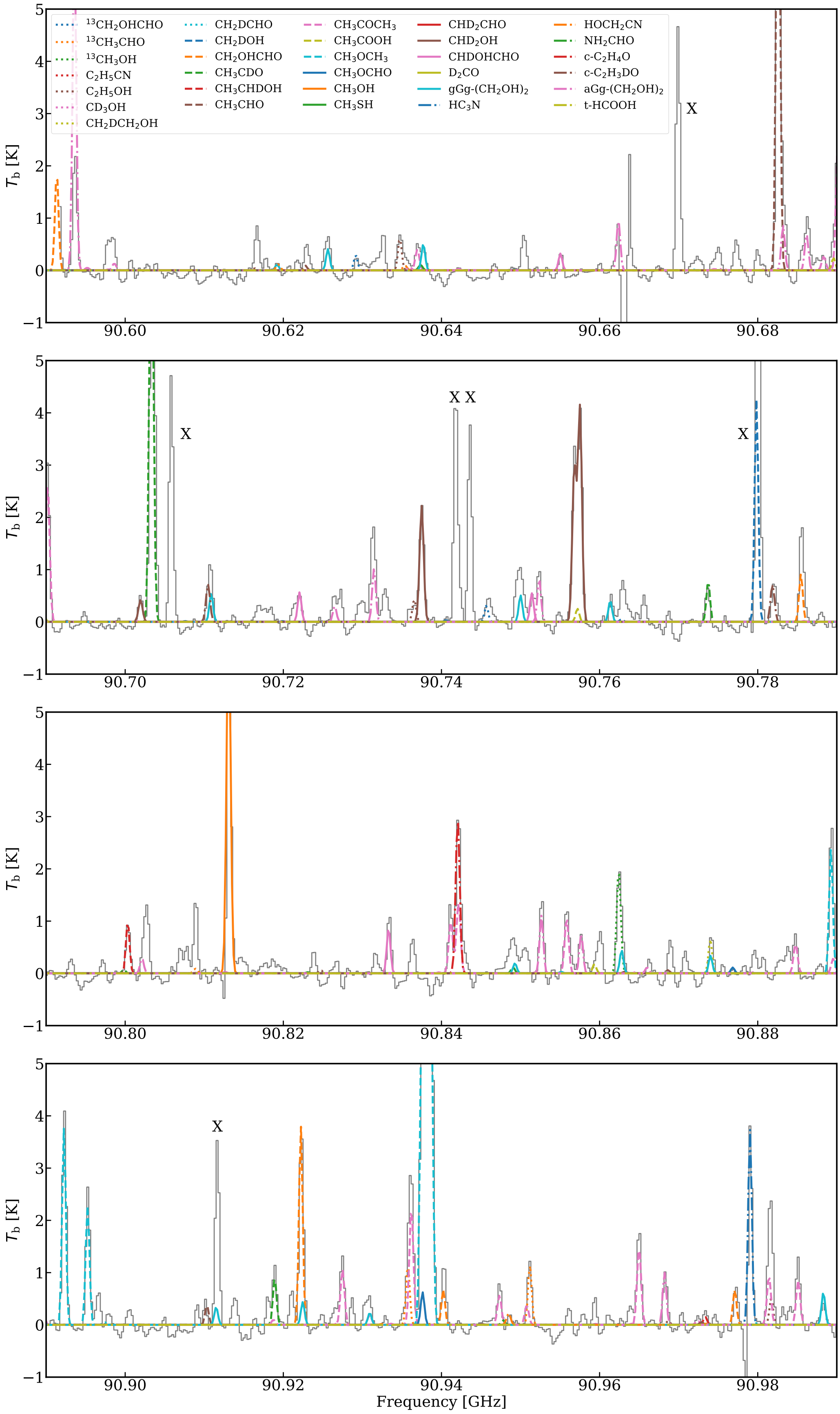

Fig. B.1: Fitted model for each molecule on top of the Band 3 data in gray. For readability, the y-axis limit was set to 5 K; however, no line was overestimated except those of methanol and one line of aGg′-$(CH_2OH)_2$, which are potentially optically thick. The lines that have an intensity higher than 2 K (i.e., detected at a $\gtrsim 7 - 10\sigma$ level) but that were not identified are indicated by an "X".

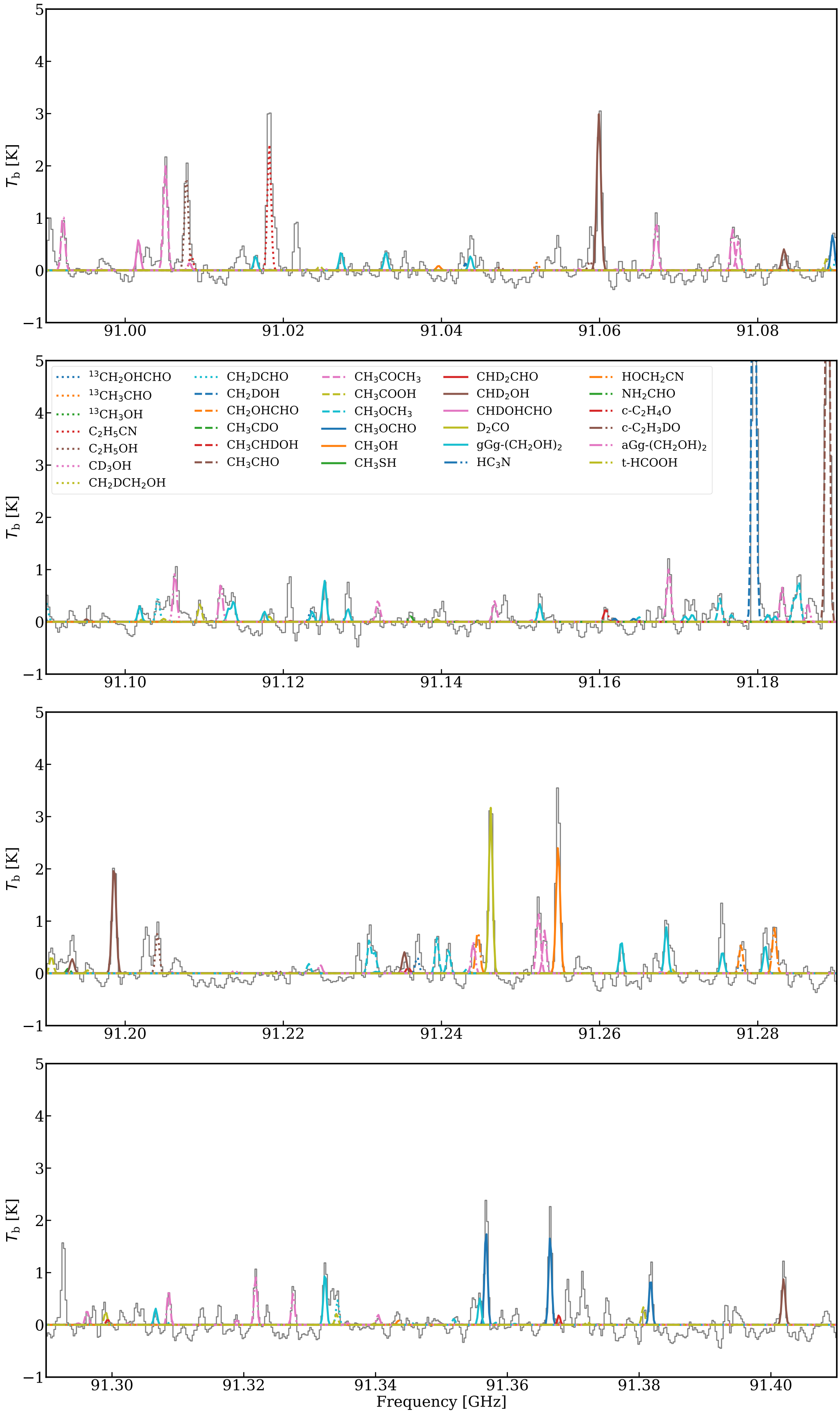

Fig. B.1: Continued

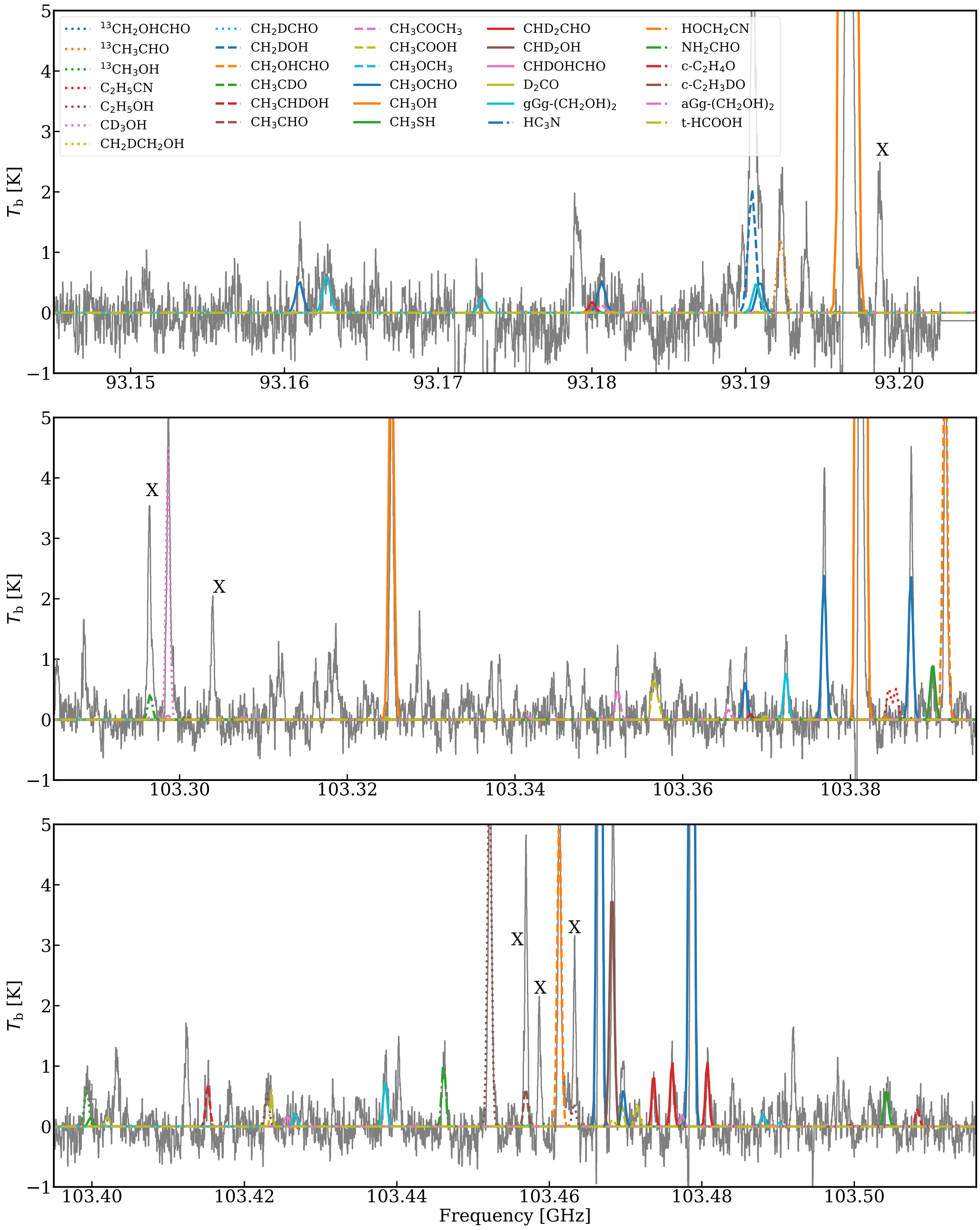

Fig. B.1: Continued

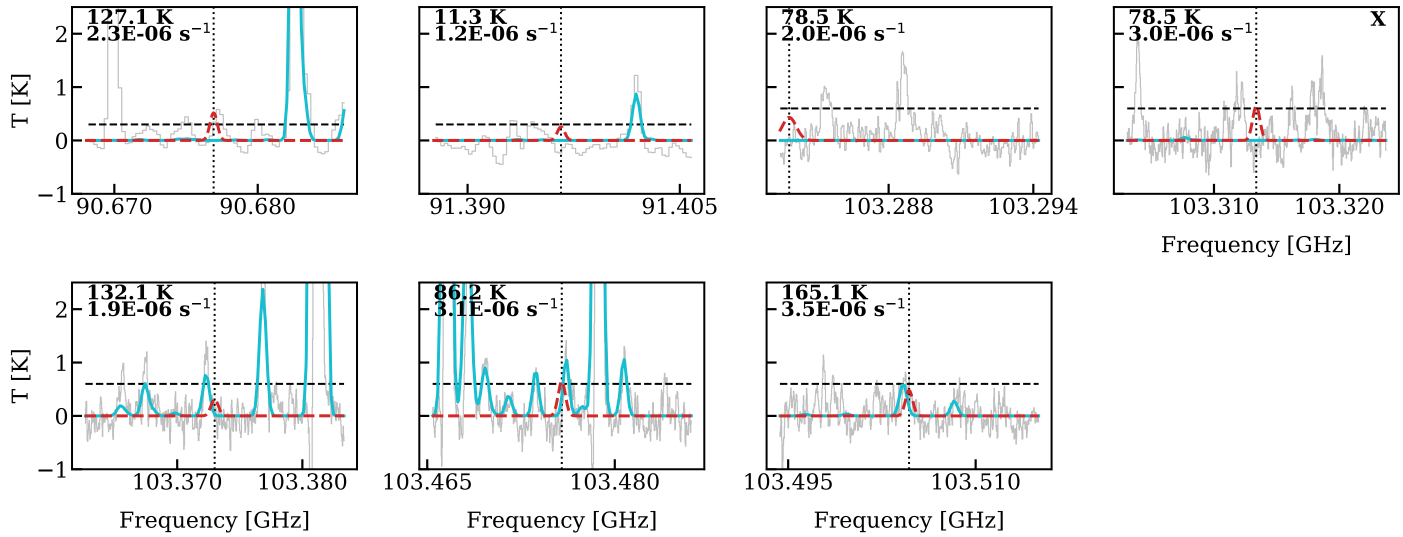

Fig. B.2: Lines of Ga-n-propanol and the model for its upper limit (6×10^{15} cm^{-2}) in red. The symbols are the same as in Fig. 3.

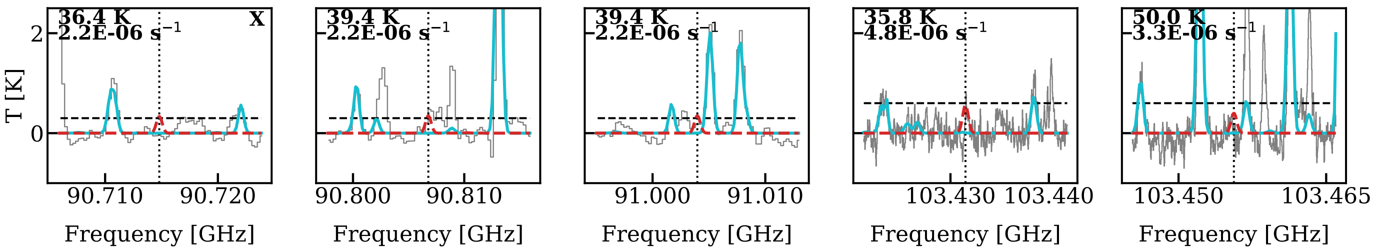

Fig. B.3: Lines of G′Gg′gg′-Glycerol and the model for its upper limit (7×10^{15} cm^{-2}) in red. The symbols are the same as in Fig. 3.

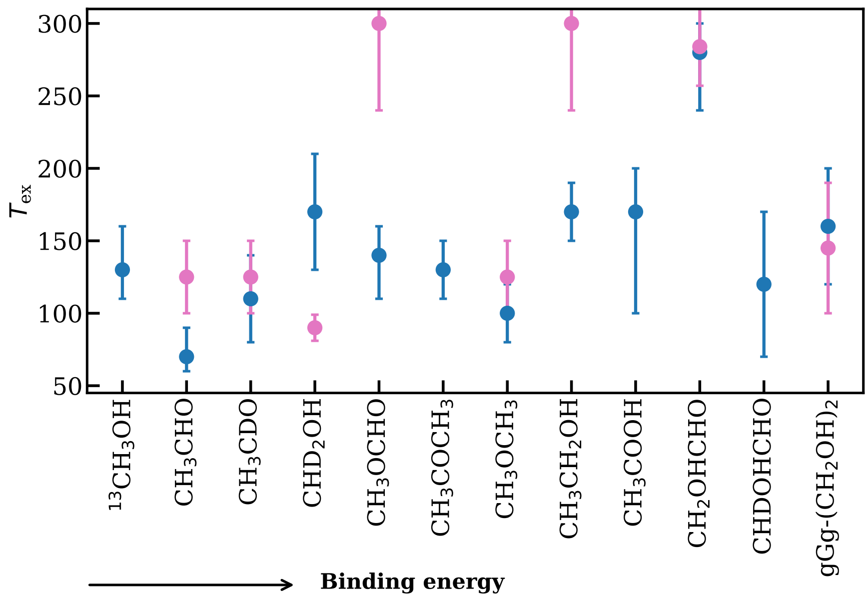

Fig. B.4: Excitation temperatures for molecules where a determination was possible. The species are ordered by their binding energies taken from Minissale et al. (2022) and Ligterink & Minissale (2023). The binding energy of the isotopologues was assumed to be the same as the major isotopologue. Band 3 results are shown in blue and Band 7 (PILS) in pink. PILS results with a fixed temperature are not shown. The temperatures for molecules from Jørgensen et al. (2018) are shown with either 300 ± 60 K or 125 ± 25 K depending on the group with which they were associated.

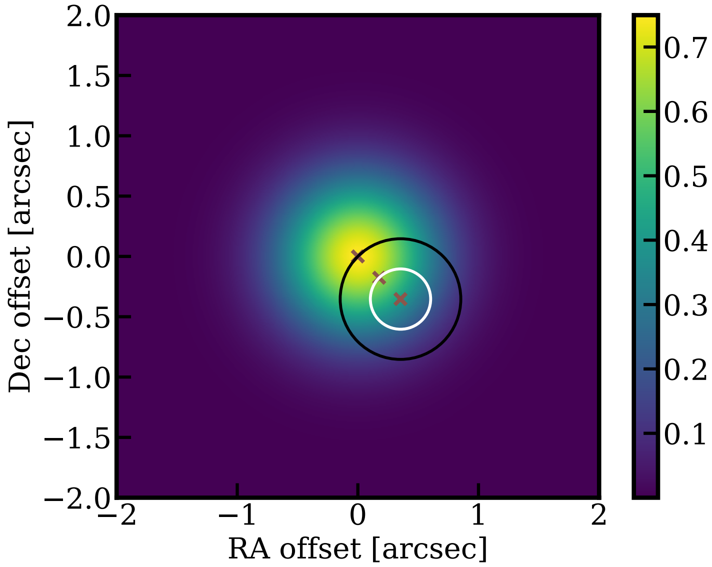

Fig. B.5: Two-dimensional Gaussian function with a total integration of one and a FWHM of 0.5″ (color scale). This was assumed as a typical emission distribution for COMs based on the results of PILS (e.g., Jørgensen et al. 2016). Two circular regions with radii of 0.25″ and 0.5″ are overplotted, representing beams of PILS (white) and Band 3 (black), respectively. The crosses show the peak position, 0.25″, and 0.5″ offset positions.

Table B.1: Upper limits of non-detections.

Name	Molecular formula	Upper limit (cm^{-2})
Methanol	$CH_3^{18}OH$	$<5.0\times10^{17}$
Formamide	NH_2CDO	$<2.0\times10^{15}$
Formamide	$NH_2^{13}CHO$	$<1.2\times10^{16}$
Formamide	cis-NHDCHO	$<2.5\times10^{15}$
Formamide	trans-NHDCHO	$<5.0\times10^{15}$
Formamide	$NH_2CHO(v_{12}=1)$	$<5.0\times10^{17}$
Z-cyanomethanimine	Z-HNCHCN	$<5.5\times10^{15}$
Methanethiol	$^{13}CH_3SH$	$<7.0\times10^{15}$
Cyanodiacetylene	HC_5N	$<2.0\times10^{13}$
Ethylene oxide	c-CD_2CH_2O	$<6.0\times10^{14}$
Acetaldehyde	$CH_3^{13}CHO$	$<6.0\times10^{15}$
Vinyl cyanide	C_2H_3CN	$<4.0\times10^{15}$
Glycolaldehyde	CH_2OHCDO	$<1.0\times10^{15}$
Glycolaldehyde	CH_2ODCHO	$<5.0\times10^{14}$
Glycolaldehyde	$CH_2OH^{13}CHO$	$<1.5\times10^{15}$
Methyl formate	$CH_3O^{13}CHO$	$<7.0\times10^{15}$
Propargyl cyanide	$HCCCH_2CN$	$<7.0\times10^{14}$
Propenal	C_2H_3CHO	$<1.5\times10^{14}$
Protonated cyanodiacetylene	HC_5NH^+	$<1.5\times10^{13}$
Urea	H_2NCONH_2	$<1.5\times10^{14}$
Ethanol	a-$^{13}CH_3CH_2OH$	$<8.0\times10^{14}$
Ethanol	a-$CH_3^{13}CH_2OH$	$<1.5\times10^{18}$
Ethanol	a-CH_3CH_2OD	$<1.0\times10^{15}$
Ethanol	a-s-CH_2DCH_2OH	$<3.0\times10^{15}$
Gauche-ethyl mercaptan	g-C_2H_5SH	$<1.0\times10^{15}$
Methoxymethanol	CH_3OCH_2OH	$<4.0\times10^{17}$
s-propanal	s-C_2H_5CHO	$<1.5\times10^{15}$
g-propanal	g-C_2H_5CHO	$<3.5\times10^{17}$
Cyclopentadiene	c-C_5H_6	$<5.0\times10^{16}$
Ethanolamine	$NH_2CH_2CH_2OH$	$<6.0\times10^{14}$
Ga-n-propanol	Ga-n-C_3H_7OH	$<6.0\times10^{15}$
Glyceraldehyde	$HCOCHOHCH_2OH$	$<8.0\times10^{15}$
g-Isopropanol	g-i-C_3H_7OH	$<1.5\times10^{16}$
a-Isopropanol	a-i-C_3H_7OH	$<2.0\times10^{16}$
Benzonitrile	c-C_6H_5CN	$<1.0\times10^{14}$
Benzaldehyde	c-C_6H_5CHO	$<7.0\times10^{14}$
GGag′g′-Glycerol	GGag′g′-$HOCH_2CH(OH)CH_2OH$	$<8.0\times10^{14}$
G′Gg′gg′-Glycerol	G′Gg′gg′-$HOCH_2CH(OH)CH_2OH$	$<7.0\times10^{15}$
Indene	c-C_9H_8	$<1.0\times10^{16}$
1-cyanonaphthalene	1-$C_{10}H_7CN$	$<1.0\times10^{14}$
2-cyanonaphthalene	2-$C_{10}H_7CN$	$<2.0\times10^{14}$

Notes. Upper limits on column densities toward the 0.5″offset position from source B in a ∼1″ beam. If a source size of 0.5″ was assumed, these values would increase by a factor of ∼5. The upper limits are measured by fixing T_{ex} to 100 K and FWHM to 2 km s^{-1}. Vibrational correction factors are not included in these values.

Table B.2: Transitions of the species studied here in the data that have E_{up} < 1000 K and $A_{ij} > 10^{-9}$ s^{-1} (not all were detected).

Species	Transition J K L M	Frequency (MHz)	A_{ij} (s^{-1})	E_{up} (K)
CH_3OH	20 3 18 5 - 19 2 18 5	90 813.078	2.80×10^{-6}	808.3
	20 2 18 2 - 20 2 19 1	91 254.751	5.29×10^{-8}	514.3
	1 0 1 4 - 2 1 2 4	93 196.672	4.19×10^{-6}	302.9
	12 3 10 1 - 13 0 13 1	103 325.252	1.81×10^{-8}	228.8
	12 2 10 2 - 12 1 11 1	103 381.258	3.98×10^{-7}	207.1
$^{13}CH_3OH$	18 -4 15 0 - 17 -5 12 0	90 862.42	1.17×10^{-6}	475.4
	8 -2 7 0 - 8 1 7 0	103 399.296	6.15×10^{-8}	107.6
CH_2DOH	22 3 19 0 - 21 4 17 2	90 762.771	5.43×10^{-8}	580.9
	2 1 1 0 - 1 1 0 0	90 779.841	1.57×10^{-6}	10.6
	25 0 25 1 - 24 3 21 2	91 043.068	2.77×10^{-7}	702.0
	9 1 8 1 - 9 0 9 1	91 179.518	2.06×10^{-6}	113.9
	29 2 28 1 - 28 4 24 2	91 392.257	1.91×10^{-8}	955.2
	28 3 25 0 - 28 3 26 0	91 395.302	9.47×10^{-8}	911.8
	18 4 14 0 - 17 5 13 0	93 190.407	1.27×10^{-6}	430.1
	26 1 25 1 - 25 4 22 1	93 193.888	2.35×10^{-9}	772.1
	18 6 12 2 - 18 6 12 1	103 347.889	1.51×10^{-9}	522.9
	18 6 13 2 - 18 6 13 1	103 347.925	1.51×10^{-9}	522.9
CHD_2OH	10 3 2 1 - 11 0 2 1	90 701.939	5.61×10^{-8}	144.1
	20 4 1 1 - 20 4 2 0	90 717.394	1.02×10^{-9}	474.9
	18 4 2 0 - 18 3 1 2	90 737.495	7.34×10^{-7}	392.4
	10 4 2 1 - 11 3 2 0	90 756.808	4.52×10^{-7}	165.0
	10 2 1 2 - 9 3 1 2	90 757.511	5.45×10^{-7}	141.1
	2 1 1 2 - 3 1 1 1	90 767.952	1.35×10^{-9}	27.7
	8 2 1 0 - 8 0 2 1	90 863.187	3.73×10^{-9}	84.9
	6 2 1 2 - 7 2 1 0	90 945.187	1.94×10^{-9}	73.2
	12 0 1 2 - 12 2 2 0	90 972.887	6.69×10^{-9}	173.9
	10 4 1 1 - 11 3 1 0	91 059.907	4.61×10^{-7}	165.0
	22 5 1 0 - 21 6 1 1	91 083.326	3.39×10^{-7}	583.4
	24 0 1 0 - 23 3 1 1	91 110.901	1.39×10^{-8}	590.9
	18 10 1 0 - 19 9 1 2	91 193.289	2.03×10^{-7}	647.5
	18 10 2 0 - 19 9 2 2	91 193.289	2.03×10^{-7}	647.5
	18 4 1 0 - 18 3 2 2	91 198.598	6.93×10^{-7}	392.4
	22 5 2 0 - 21 6 2 1	91 235.311	3.40×10^{-7}	583.5
	12 2 2 0 - 12 1 1 1	91 401.917	1.16×10^{-7}	169.5
	10 3 1 2 - 11 2 1 1	103 468.208	7.46×10^{-7}	156.7
	6 1 2 2 - 7 1 2 0	103 504.343	3.22×10^{-9}	63.3
CD_3OH	10 4 6 1 - 11 3 8 1	103 298.627	1.47×10^{-6}	156.5
CH_3CHO	25 3 23 3 - 26 0 26 3	90 618.941	2.12×10^{-8}	526.0
	7 3 5 4 - 8 2 7 4	90 622.765	5.86×10^{-7}	250.3
	4 2 3 1 - 5 0 5 2	90 636.495	3.21×10^{-9}	18.3
	34 4 30 8 - 35 2 34 7	90 670.793	8.13×10^{-9}	970.9
	11 1 10 2 - 11 0 11 2	90 682.574	3.14×10^{-6}	64.9
	28 5 23 3 - 29 3 26 3	90 723.537	1.86×10^{-8}	636.9
	31 2 29 0 - 32 0 32 0	90 730.219	2.82×10^{-9}	475.7
	13 2 11 6 - 14 1 14 6	90 731.485	6.83×10^{-7}	471.1
	37 4 33 5 - 37 4 34 4	90 737.826	3.52×10^{-7}	897.9
	21 6 15 5 - 22 5 17 5	90 743.918	6.78×10^{-7}	500.7
	35 4 32 4 - 36 2 35 4	90 746.919	3.37×10^{-9}	825.9
	29 3 27 4 - 29 2 27 5	90 791.888	1.23×10^{-9}	628.4
	21 2 19 6 - 22 1 22 6	90 856.686	3.05×10^{-7}	604.1
	9 0 9 5 - 8 1 7 5	90 868.634	2.84×10^{-7}	245.7
	28 2 26 2 - 27 4 23 2	90 905.459	2.57×10^{-8}	391.5
	5 0 5 8 - 4 0 4 8	90 910.33	2.42×10^{-5}	391.6
	24 4 20 8 - 24 4 21 7	90 999.685	4.68×10^{-8}	693.0
	40 5 36 0 - 41 2 39 0	91 005.733	6.98×10^{-8}	817.0
	17 2 16 3 - 16 3 13 3	91 095.085	5.97×10^{-7}	355.3

Table B.2: continued.

Species	Transition J K L M	Frequency (MHz)	A_{ij} (s^{-1})	E_{up} (K)
	30 3 28 7 - 31 0 31 8	91 155.32	5.90×10^{-9}	829.2
	11 1 10 0 - 11 0 11 0	91 188.823	3.22×10^{-6}	64.8
	36 4 33 4 - 37 2 36 4	91 189.824	3.10×10^{-9}	859.3
	34 4 31 4 - 35 2 34 4	91 213.789	3.73×10^{-9}	793.4
	31 5 27 0 - 30 6 24 0	91 296.802	7.77×10^{-7}	516.1
	20 1 19 8 - 19 3 17 7	93 202.965	6.38×10^{-9}	581.1
	33 4 30 1 - 34 2 33 1	103 321.687	1.06×10^{-8}	556.4
	5 2 4 7 - 4 1 3 8	103 326.134	2.76×10^{-9}	401.5
	33 2 32 0 - 32 3 29 0	103 354.087	1.84×10^{-7}	520.8
	34 4 31 1 - 35 2 34 1	103 378.41	1.03×10^{-8}	587.9
	32 2 30 5 - 33 0 33 5	103 395.991	3.64×10^{-9}	711.1
	36 5 32 1 - 37 3 35 1	103 429.039	1.42×10^{-8}	674.0
	11 2 9 3 - 11 1 10 3	103 456.903	4.86×10^{-6}	275.9
	30 8 23 3 - 31 7 24 3	103 489.605	9.90×10^{-7}	779.4
	30 8 22 3 - 31 7 25 3	103 496.344	9.90×10^{-7}	779.4
$^{13}CH_3CHO$	37 6 32 -3 - 36 7 29 -3	90 765.097	7.94×10^{-7}	918.8
	27 7 21 -3 - 28 6 22 -3	90 791.095	7.33×10^{-7}	655.2
	16 2 14 1 - 15 3 12 1	90 802.2	6.92×10^{-8}	132.8
	27 7 20 -3 - 28 6 23 -3	90 830.059	7.34×10^{-7}	655.2
	22 3 20 -3 - 23 0 23 -3	90 904.355	2.60×10^{-8}	452.6
	5 1 5 0 - 4 1 4 0	90 935.753	2.41×10^{-5}	15.4
	5 1 5 1 - 4 1 4 1	90 951.18	2.41×10^{-5}	15.4
	33 4 30 -3 - 34 2 33 -3	90 961.839	1.73×10^{-8}	746.1
	5 1 5 -3 - 4 1 4 -3	91 052.078	2.44×10^{-5}	221.8
	34 4 31 -3 - 35 2 34 -3	91 058.163	1.68×10^{-8}	776.8
	29 2 27 -2 - 28 4 24 -2	91 172.915	1.78×10^{-8}	612.2
	25 3 23 -3 - 26 0 26 -3	91 232.409	2.32×10^{-8}	517.4
	29 3 26 -3 - 29 3 27 -3	91 304.282	6.05×10^{-7}	620.5
	5 2 4 1 - 4 2 2 1	91 305.92	1.01×10^{-7}	22.5
	23 1 22 1 - 22 3 19 1	91 313.98	3.30×10^{-8}	253.5
	32 5 28 0 - 31 6 25 0	91 370.438	8.31×10^{-7}	531.6
	11 2 10 -2 - 11 1 10 -2	91 386.732	7.84×10^{-7}	272.2
	39 5 35 0 - 40 3 38 0	91 395.629	8.97×10^{-9}	758.9
	36 9 27 -3 - 37 8 29 -3	93 187.027	8.16×10^{-7}	985.7
	5 0 5 1 - 4 0 4 1	93 192.298	2.70×10^{-5}	13.5
	36 9 28 -3 - 37 8 30 -3	93 194.864	8.16×10^{-7}	985.7
	39 4 36 -3 - 40 2 39 -3	103 353.904	2.05×10^{-8}	943.5
	18 3 16 -3 - 19 0 19 -3	103 463.152	4.01×10^{-8}	378.7
	38 5 34 -2 - 39 2 37 -2	103 484.196	7.87×10^{-8}	928.7
	12 2 10 -3 - 12 1 11 -3	103 487.851	5.26×10^{-6}	285.2
CH_3CDO	5 1 5 0 - 4 1 4 0	90 703.205	2.39×10^{-5}	14.8
	5 1 5 1 - 4 1 4 1	90 703.424	2.39×10^{-5}	14.8
	16 3 13 5 - 15 4 12 4	90 707.948	5.88×10^{-8}	341.0
	5 1 5 3 - 4 1 4 3	90 773.736	2.41×10^{-5}	216.4
	4 2 2 3 - 4 1 3 3	90 799.825	2.55×10^{-6}	217.0
	22 2 21 1 - 21 3 18 2	90 823.11	2.02×10^{-7}	232.9
	10 1 9 5 - 10 0 10 5	90 849.045	2.77×10^{-6}	253.5
	8 2 6 0 - 8 1 7 0	90 918.912	3.66×10^{-6}	39.8
	14 3 12 3 - 15 0 15 3	90 926.592	2.93×10^{-8}	311.4
	17 2 16 1 - 16 3 13 2	90 947.817	4.54×10^{-7}	144.3
	11 5 6 2 - 12 4 8 2	91 192.805	5.21×10^{-7}	102.6
	15 2 14 4 - 14 3 12 4	91 214.539	3.12×10^{-7}	315.3
	22 8 14 5 - 23 7 16 5	91 278.766	6.04×10^{-7}	539.7
	25 12 13 2 - 24 6 19 4	103 300.073	9.11×10^{-7}	539.8
	16 11 6 1 - 15 3 13 4	103 316.694	3.40×10^{-7}	329.6
	2 2 1 4 - 2 1 2 4	103 470.435	2.49×10^{-6}	209.1

Table B.2: continued.

Species	Transition J K L M	Frequency (MHz)	A_{ij} (s^{-1})	E_{up} (K)
CH_2DCHO	6 3 4 2 - 7 2 6 1	90 671.76	1.70×10^{-7}	59.2
	5 2 3 1 - 4 2 3 2	90 897.364	4.40×10^{-7}	43.7
	5 2 3 2 - 4 2 3 1	90 979.724	2.97×10^{-7}	43.7
	3 1 3 0 - 2 0 2 0	91 090.016	3.43×10^{-6}	7.0
	13 1 12 2 - 13 0 13 2	91 104.13	3.02×10^{-6}	104.7
	18 2 16 0 - 18 2 17 0	91 308.321	5.09×10^{-7}	162.7
	13 1 12 1 - 13 0 13 1	91 334.229	3.06×10^{-6}	104.6
	6 3 4 1 - 7 2 6 2	91 344.243	5.69×10^{-8}	59.3
	25 8 18 0 - 26 7 19 0	103 303.817	1.11×10^{-6}	409.4
	25 8 17 0 - 26 7 20 0	103 308.431	1.11×10^{-6}	409.4
	16 4 12 0 - 17 2 15 0	103 450.4	1.69×10^{-8}	151.2
	11 2 10 1 - 11 1 10 2	103 463.833	1.35×10^{-8}	87.7
CHD_2CHO	6 1 5 2 - 5 1 4 2	103 473.67	3.75×10^{-9}	40.1
	6 0 6 1 - 5 0 5 1	103 476.11	3.72×10^{-9}	17.4
	6 0 6 0 - 5 0 5 0	103 480.72	3.72×10^{-9}	17.4
CH_3CH_2OH	39 13 27 1 - 38 14 25 0	90 616.41	4.90×10^{-7}	916.5
	39 13 26 1 - 38 14 24 0	90 616.41	4.90×10^{-7}	916.5
	39 3 36 1 - 39 4 36 0	90 634.74	5.11×10^{-6}	728.3
	47 1 46 2 - 46 1 46 1	90 673.782	1.70×10^{-8}	916.6
	47 1 46 2 - 46 0 46 1	90 673.816	3.95×10^{-8}	916.6
	47 2 46 2 - 46 1 46 1	90 674.536	3.95×10^{-8}	916.6
	47 2 46 2 - 46 0 46 1	90 674.571	1.70×10^{-8}	916.6
	42 5 38 1 - 43 5 38 2	90 701.878	1.88×10^{-8}	844.8
	31 8 24 2 - 30 6 24 1	90 724.54	2.48×10^{-8}	497.7
	28 12 17 2 - 29 11 18 2	90 736.55	7.33×10^{-7}	521.5
	28 12 16 2 - 29 11 19 2	90 736.571	7.33×10^{-7}	521.5
	38 6 33 1 - 39 7 33 2	90 809.192	1.68×10^{-8}	724.0
	19 3 16 1 - 19 2 17 1	90 824.709	5.78×10^{-8}	232.3
	21 20 1 2 - 21 19 2 0	90 947.962	6.04×10^{-8}	694.1
	21 20 2 2 - 21 19 3 0	90 947.962	6.04×10^{-8}	694.1
	21 2 19 1 - 21 2 19 0	90 968.68	7.21×10^{-8}	262.0
	7 2 6 1 - 6 3 4 0	90 981.716	5.24×10^{-7}	89.7
	29 2 27 1 - 29 7 23 2	90 992.97	8.40×10^{-8}	432.1
	14 2 13 2 - 13 3 10 2	91 007.739	9.91×10^{-7}	92.6
	36 10 27 1 - 35 11 24 1	91 030.651	3.31×10^{-8}	737.8
	36 10 26 1 - 35 11 25 1	91 030.969	3.31×10^{-8}	737.8
	18 3 15 1 - 18 2 16 1	91 047.417	5.85×10^{-8}	216.2
	25 2 24 2 - 24 3 21 2	91 058.798	1.52×10^{-7}	272.8
	25 11 15 2 - 26 10 16 2	91 204.078	8.20×10^{-7}	424.7
	25 11 14 2 - 26 10 17 2	91 204.079	8.20×10^{-7}	424.7
	20 3 17 1 - 20 3 17 0	91 219.35	5.52×10^{-8}	249.4
	7 2 6 0 - 7 1 7 0	91 241.609	7.12×10^{-9}	84.9
	30 3 28 2 - 31 0 31 2	91 250.931	1.83×10^{-8}	399.7
	38 16 22 1 - 38 16 22 0	91 332.886	8.06×10^{-8}	990.3
	38 16 23 1 - 38 16 23 0	91 332.886	8.06×10^{-8}	990.3
	31 8 23 2 - 30 6 25 1	93 145.898	3.66×10^{-8}	497.7
	35 10 26 2 - 34 9 25 0	93 180.157	6.27×10^{-9}	655.1
	35 10 25 2 - 34 9 26 0	93 183.533	6.27×10^{-9}	655.1
	25 6 20 1 - 25 6 20 0	103 300.62	4.91×10^{-9}	376.3
	7 0 7 0 - 6 1 6 0	103 300.759	6.84×10^{-8}	79.9
	4 2 3 1 - 4 0 4 1	103 320.469	1.28×10^{-8}	74.8
	34 8 26 1 - 34 8 26 0	103 381.264	9.03×10^{-9}	635.1
	34 8 27 1 - 34 8 27 0	103 385.983	8.98×10^{-9}	635.1
	9 2 8 1 - 9 1 9 1	103 387.337	2.99×10^{-8}	103.7
	37 9 28 1 - 37 9 28 0	103 403.957	2.12×10^{-8}	745.6
	37 9 29 1 - 37 9 29 0	103 404.936	2.12×10^{-8}	745.6

Table B.2: continued.

Species	Transition J K L M	Frequency (MHz)	A_{ij} (s^{-1})	E_{up} (K)
	27 5 22 0 - 26 6 20 1	103 422.99	1.25×10^{-6}	403.0
	15 2 13 0 - 15 0 15 1	103 431.155	1.90×10^{-8}	163.3
	6 2 5 0 - 5 2 4 0	103 452.151	8.32×10^{-6}	79.2
	38 11 27 1 - 38 11 27 0	103 457.114	1.75×10^{-8}	825.6
	38 11 28 1 - 38 11 28 0	103 457.118	1.75×10^{-8}	825.6
	6 2 5 0 - 6 0 6 0	103 463.245	5.33×10^{-7}	79.2
	6 0 6 2 - 5 0 5 2	103 480.355	1.26×10^{-8}	17.5
	9 1 8 0 - 8 2 7 0	103 488.524	7.92×10^{-8}	96.5
CH_2DCH_2OH	44 3 41 - 43 6 38	90 856.753	1.14×10^{-7}	811.0
	8 2 7 - 8 1 8	90 874.001	3.63×10^{-6}	33.4
CH_3CHDOH	46 6 40 - 45 9 37	90 764.508	9.58×10^{-8}	946.6
	11 3 8 - 11 2 9	90 800.322	5.71×10^{-6}	64.1
	13 2 12 - 12 3 9	90 973.356	8.44×10^{-7}	78.6
	5 5 1 - 6 4 2	91 219.103	1.43×10^{-7}	38.3
	5 5 0 - 6 4 3	91 220.883	1.43×10^{-7}	38.3
	15 9 7 - 16 8 8	91 235.784	5.29×10^{-7}	183.0
	15 9 6 - 16 8 9	91 235.788	5.29×10^{-7}	183.0
	10 7 4 - 11 6 5	91 299.292	4.07×10^{-7}	96.2
	10 7 3 - 11 6 6	91 299.396	4.07×10^{-7}	96.2
	7 3 4 - 7 2 5	103 415.2	6.61×10^{-6}	32.5
	20 2 19 - 19 3 16	103 499.655	3.16×10^{-7}	174.2
	11 2 9 - 10 3 8	103 508.282	2.08×10^{-6}	59.8
CH_3OCHO	27 16 12 4 - 28 15 14 4	90 592.278	1.03×10^{-7}	580.3
	23 3 20 0 - 24 2 23 0	90 649.201	7.44×10^{-9}	173.2
	33 19 14 2 - 34 18 16 2	90 707.602	1.06×10^{-7}	570.2
	33 19 15 1 - 34 18 17 1	90 719.908	1.06×10^{-7}	570.2
	33 19 14 0 - 34 18 17 0	90 740.574	1.06×10^{-7}	570.2
	33 19 15 0 - 34 18 16 0	90 740.574	1.06×10^{-7}	570.2
	9 4 6 1 - 9 3 6 2	90 876.84	6.31×10^{-8}	37.2
	17 3 14 5 - 17 2 15 5	90 937.614	1.13×10^{-6}	286.2
	27 16 11 5 - 28 15 13 5	91 018.326	1.04×10^{-7}	580.5
	19 5 14 5 - 19 4 15 5	91 089.478	1.38×10^{-6}	316.9
	36 5 31 3 - 35 7 28 3	91 134.07	2.89×10^{-8}	603.3
	26 8 19 3 - 25 9 16 3	91 161.894	2.21×10^{-7}	437.0
	26 8 18 5 - 25 9 16 5	91 164.314	2.14×10^{-7}	437.1
	36 20 16 5 - 37 19 18 5	91 179.846	1.14×10^{-7}	845.3
	34 6 29 0 - 35 4 32 0	91 179.968	8.61×10^{-9}	377.6
	34 6 29 0 - 35 3 32 0	91 194.313	1.29×10^{-8}	377.6
	9 4 5 0 - 9 3 6 0	91 356.766	1.03×10^{-6}	37.2
	9 4 5 2 - 9 3 6 2	91 366.495	9.71×10^{-7}	37.3
	14 2 12 2 - 14 2 13 1	91 381.738	4.08×10^{-7}	67.0
	10 3 8 1 - 10 1 9 2	93 160.968	2.82×10^{-7}	38.5
	12 3 10 3 - 12 2 11 3	93 180.635	9.90×10^{-7}	239.5
	10 3 8 0 - 10 1 9 0	93 190.933	2.83×10^{-7}	38.5
	43 15 29 4 - 42 16 27 4	103 307.836	2.85×10^{-7}	893.2
	32 19 13 2 - 33 18 15 2	103 335.016	1.47×10^{-7}	550.7
	32 19 14 1 - 33 18 16 1	103 342.834	1.47×10^{-7}	550.7
	25 6 19 5 - 25 5 20 5	103 367.418	2.23×10^{-6}	405.1
	32 19 13 0 - 33 18 16 0	103 367.795	1.47×10^{-7}	550.7
	32 19 14 0 - 33 18 15 0	103 367.795	1.47×10^{-7}	550.7
	24 6 18 0 - 24 5 19 0	103 376.842	2.21×10^{-6}	203.8
	24 6 18 2 - 24 5 19 2	103 387.2	2.21×10^{-6}	203.8
	36 12 24 5 - 35 13 22 5	103 456.449	3.03×10^{-7}	675.5
	8 2 6 2 - 7 2 5 2	103 466.572	1.52×10^{-5}	24.6
	25 6 19 3 - 25 5 20 3	103 469.71	2.28×10^{-6}	405.0
	8 2 6 0 - 7 2 5 0	103 478.663	1.52×10^{-5}	24.6

Table B.2: continued.

Species	Transition J K L M	Frequency (MHz)	A_{ij} (s^{-1})	E_{up} (K)
CH_3OCH_3	15 3 12 0 - 14 4 11 0	90 889.262	1.02×10^{-6}	122.5
	15 3 12 1 - 14 4 11 1	90 892.26	1.02×10^{-6}	122.5
	15 3 12 5 - 14 4 11 5	90 895.187	1.02×10^{-6}	122.5
	15 3 12 3 - 14 4 11 3	90 895.33	1.02×10^{-6}	122.5
	6 0 6 0 - 5 1 5 0	90 937.508	3.63×10^{-6}	19.0
	6 0 6 1 - 5 1 5 1	90 938.107	3.63×10^{-6}	19.0
	6 0 6 5 - 5 1 5 5	90 938.705	3.63×10^{-6}	19.0
	6 0 6 3 - 5 1 5 3	90 938.707	3.63×10^{-6}	19.0
	5 3 2 3 - 6 4 2 3	91 164.996	1.15×10^{-7}	36.1
	5 3 2 1 - 6 4 3 1	91 175.203	1.44×10^{-7}	36.1
	5 3 2 5 - 6 4 3 5	91 176.676	3.45×10^{-7}	36.1
	5 3 2 0 - 6 4 3 0	91 184.531	3.46×10^{-7}	36.1
	5 3 2 3 - 6 4 3 3	91 185.031	2.31×10^{-7}	36.2
	5 3 2 1 - 6 4 2 1	91 185.221	2.02×10^{-7}	36.1
	5 3 3 3 - 6 4 2 3	91 223.214	2.31×10^{-7}	36.1
	5 3 3 1 - 6 4 3 1	91 230.878	2.02×10^{-7}	36.1
	5 3 3 5 - 6 4 2 5	91 231.569	3.46×10^{-7}	36.1
	5 3 3 0 - 6 4 2 0	91 239.423	3.47×10^{-7}	36.1
	5 3 3 1 - 6 4 2 1	91 240.896	1.44×10^{-7}	36.1
	5 3 3 3 - 6 4 3 3	91 243.249	1.16×10^{-7}	36.2
	9 0 9 3 - 10 3 8 3	91 345.408	2.47×10^{-8}	53.6
	9 0 9 5 - 10 3 8 5	91 345.55	2.47×10^{-8}	53.6
	9 0 9 1 - 10 3 8 1	91 351.871	2.51×10^{-8}	53.6
	9 0 9 0 - 10 3 8 0	91 358.263	2.53×10^{-8}	53.6
	32 12 20 3 - 33 13 20 3	103 489.911	1.08×10^{-6}	717.6
	32 12 21 1 - 33 13 21 1	103 489.975	1.08×10^{-6}	717.6
	32 12 20 0 - 33 13 21 0	103 490.039	1.08×10^{-6}	717.6
	32 12 21 0 - 33 13 20 0	103 490.039	1.08×10^{-6}	717.6
	32 12 20 5 - 33 13 21 5	103 490.157	1.08×10^{-6}	717.6
	32 12 21 5 - 33 13 20 5	103 490.157	1.08×10^{-6}	717.6
	32 12 20 1 - 33 13 20 1	103 490.221	1.08×10^{-6}	717.6
	32 12 21 3 - 33 13 21 3	103 490.403	1.08×10^{-6}	717.6
CH_3COCH_3	41 27 14 0 - 41 26 15 0	90 595.197	2.62×10^{-5}	708.7
	20 17 3 2 - 20 16 4 2	90 598.617	1.28×10^{-5}	186.7
	20 17 4 2 - 20 16 5 2	90 636.946	1.29×10^{-5}	186.7
	20 17 3 3 - 20 16 4 3	90 688.355	1.29×10^{-5}	186.8
	13 3 10 1 - 13 2 11 1	90 690.157	9.47×10^{-6}	59.9
	13 4 10 1 - 13 3 11 1	90 690.212	9.47×10^{-6}	59.9
	9 7 2 3 - 8 8 0 3	90 808.887	4.05×10^{-7}	38.5
	27 19 8 1 - 27 18 10 1	90 812.649	6.42×10^{-7}	315.8
	12 2 10 2 - 12 1 11 2	90 841.133	7.02×10^{-6}	48.5
	12 3 10 2 - 12 2 11 2	90 841.14	7.02×10^{-6}	48.5
	12 2 10 3 - 12 1 11 3	90 841.209	7.02×10^{-6}	48.5
	12 3 10 3 - 12 2 11 3	90 841.217	7.02×10^{-6}	48.5
	13 3 10 0 - 13 2 11 0	90 842.133	9.52×10^{-6}	59.8
	13 4 10 0 - 13 3 11 0	90 842.19	9.53×10^{-6}	59.8
	20 17 4 1 - 20 16 5 1	90 855.834	1.29×10^{-5}	186.7
	13 6 7 1 - 12 9 4 1	90 879.456	1.57×10^{-7}	70.3
	7 3 5 3 - 6 2 4 3	90 884.785	2.10×10^{-5}	19.7
	7 3 5 2 - 6 2 4 2	90 889.558	2.10×10^{-5}	19.7
	20 17 3 1 - 20 16 4 1	90 927.486	1.29×10^{-5}	186.8
	26 19 8 3 - 26 18 9 3	90 930.919	1.63×10^{-5}	296.2
	7 3 5 1 - 6 2 4 1	90 936.196	2.10×10^{-5}	19.6
	23 12 11 2 - 23 11 12 2	90 947.328	2.04×10^{-5}	218.4
	23 12 11 3 - 23 11 12 3	90 950.792	2.04×10^{-5}	218.4
	27 19 8 3 - 27 18 10 3	90 959.492	1.83×10^{-6}	315.8

Table B.2: continued.

Species	Transition J K L M	Frequency (MHz)	A_{ij} (s^{-1})	E_{up} (K)
	23 12 11 1 - 23 11 12 1	90 964.992	2.04×10^{-5}	218.4
	9 7 3 3 - 8 8 1 3	90 965.369	4.04×10^{-7}	38.3
	41 27 14 1 - 41 26 15 1	90 972.394	2.64×10^{-5}	708.7
	22 8 14 1 - 21 11 11 1	90 977.509	7.34×10^{-8}	183.5
	23 12 11 0 - 23 11 12 0	90 981.426	2.04×10^{-5}	218.4
	7 3 5 0 - 6 2 4 0	90 985.117	2.10×10^{-5}	19.5
	12 2 10 1 - 12 1 11 1	91 005.085	7.06×10^{-6}	48.4
	12 3 10 1 - 12 2 11 1	91 005.092	7.06×10^{-6}	48.4
	9 7 2 1 - 8 8 0 1	91 057.153	3.53×10^{-7}	38.4
	11 1 10 2 - 11 0 11 2	91 077.508	3.96×10^{-6}	37.8
	11 2 10 2 - 11 1 11 2	91 077.509	3.96×10^{-6}	37.8
	11 1 10 3 - 11 0 11 3	91 077.598	3.96×10^{-6}	37.8
	11 2 10 3 - 11 1 11 3	91 077.598	3.96×10^{-6}	37.8
	23 18 5 2 - 23 17 6 2	91 131.97	1.70×10^{-5}	238.0
	22 9 14 1 - 21 10 11 1	91 132.382	7.38×10^{-8}	183.5
	20 17 3 0 - 20 16 4 0	91 146.721	1.30×10^{-5}	186.7
	12 2 10 0 - 12 1 11 0	91 168.75	7.11×10^{-6}	48.3
	12 3 10 0 - 12 2 11 0	91 168.757	7.11×10^{-6}	48.3
	20 17 4 0 - 20 16 5 0	91 183.074	1.30×10^{-5}	186.7
	41 25 16 2 - 41 24 17 2	91 202.244	2.72×10^{-5}	700.6
	41 25 16 3 - 41 24 17 3	91 205.905	2.72×10^{-5}	700.6
	11 1 10 1 - 11 0 11 1	91 252.28	3.99×10^{-6}	37.7
	11 2 10 1 - 11 1 11 1	91 252.281	3.99×10^{-6}	37.7
	41 27 14 2 - 41 26 15 2	91 294.888	2.67×10^{-5}	708.7
	23 18 6 3 - 23 17 7 3	91 296.205	1.70×10^{-5}	237.9
	41 25 16 1 - 41 24 17 1	91 318.968	2.73×10^{-5}	700.7
	41 27 14 3 - 41 26 15 3	91 393.556	2.66×10^{-5}	708.7
	9 6 4 3 - 8 7 1 3	93 175.842	5.69×10^{-7}	36.6
	25 19 7 1 - 25 18 7 1	93 183.007	1.96×10^{-6}	277.6
	8 5 3 1 - 8 2 6 1	103 297.162	1.37×10^{-7}	29.4
	31 22 10 2 - 31 21 11 2	103 298.616	3.10×10^{-5}	415.4
	24 10 15 1 - 23 11 12 1	103 309.761	1.14×10^{-7}	219.0
	31 22 10 1 - 31 21 11 1	103 352.24	3.07×10^{-5}	415.4
	42 28 14 1 - 42 27 15 1	103 365.841	3.62×10^{-5}	745.1
	31 22 10 0 - 31 21 11 0	103 425.624	3.11×10^{-5}	415.5
CH_3COOH	9 5 4 0 0 - 8 7 1 0 0	90 619.38	1.29×10^{-8}	40.6
	21 13 9 0 2 - 20 16 4 0 1	90 638.822	4.29×10^{-9}	207.8
	22 8 14 0 1 - 21 10 11 0 2	90 670.076	4.28×10^{-9}	203.4
	22 9 14 0 1 - 21 10 11 0 2	90 670.227	1.80×10^{-8}	203.4
	23 17 6 0 1 - 23 16 7 0 2	90 689.582	4.84×10^{-6}	260.4
	35 13 23 0 2 - 34 15 20 0 1	90 716.134	2.96×10^{-9}	496.3
	35 12 23 0 2 - 34 15 20 0 1	90 716.134	1.12×10^{-8}	496.3
	35 12 23 0 2 - 34 14 20 0 1	90 716.15	2.96×10^{-9}	496.3
	35 13 23 0 2 - 34 14 20 0 1	90 716.15	1.12×10^{-8}	496.3
	8 6 2 0 0 - 8 4 5 0 0	90 727.049	2.18×10^{-8}	34.4
	6 3 4 0 1 - 5 2 3 0 2	90 757.201	4.46×10^{-6}	17.0
	13 7 7 0 0 - 12 9 3 0 0	90 762.796	2.50×10^{-9}	78.4
	9 3 6 0 0 - 8 4 4 0 0	90 771.09	2.25×10^{-9}	36.3
	36 26 10 0 0 - 35 29 6 0 0	90 852.622	1.11×10^{-9}	623.9
	27 19 8 0 1 - 27 18 9 0 2	90 859.346	5.46×10^{-6}	351.7
	10 8 3 0 0 - 10 5 5 0 0	90 898.339	1.21×10^{-7}	52.9
	8 6 2 0 0 - 7 7 0 0 0	90 901.78	1.30×10^{-7}	34.4
	25 13 13 0 0 - 24 16 8 0 0	90 917.361	3.12×10^{-9}	280.1
	22 14 9 0 2 - 21 17 4 0 1	90 947.862	3.54×10^{-9}	229.2
	35 19 16 0 0 - 34 24 11 0 0	90 949.971	1.58×10^{-9}	558.0
	15 9 6 0 0 - 14 12 2 0 0	90 983.691	3.65×10^{-9}	108.9

Table B.2: continued.

Species	Transition J K L M	Frequency (MHz)	A_{ij} (s^{-1})	E_{up} (K)
	44 28 16 0 0 - 44 27 17 0 0	90 987.155	7.54×10^{-6}	901.4
	4 3 1 0 2 - 3 2 2 0 1	91 024.622	1.97×10^{-6}	9.4
	7 5 2 0 0 - 7 3 5 0 0	91 062.482	1.18×10^{-8}	26.6
	8 6 2 0 0 - 8 3 5 0 0	91 071.232	1.01×10^{-7}	34.4
	12 8 5 0 0 - 11 10 2 0 0	91 077.987	2.76×10^{-9}	71.2
	23 17 7 0 0 - 23 16 8 0 0	91 088.715	4.68×10^{-6}	259.9
	38 25 13 0 2 - 38 24 14 0 1	91 102.138	6.82×10^{-6}	678.6
	16 7 9 0 0 - 16 7 10 0 0	91 104.88	7.50×10^{-7}	115.2
	16 7 9 0 0 - 16 6 10 0 0	91 109.457	4.22×10^{-6}	115.2
	33 20 13 0 2 - 33 19 14 0 1	91 118.246	6.41×10^{-6}	507.8
	22 12 10 0 1 - 22 12 11 0 2	91 139.444	8.11×10^{-7}	224.9
	7 5 2 0 0 - 7 2 5 0 0	91 145.635	5.62×10^{-8}	26.6
	9 7 2 0 1 - 9 5 5 0 2	91 159.53	5.66×10^{-8}	42.9
	16 8 9 0 0 - 16 7 10 0 0	91 190.673	4.23×10^{-6}	115.2
	16 8 9 0 0 - 16 6 10 0 0	91 195.251	7.52×10^{-7}	115.2
	8 4 4 0 0 - 7 6 2 0 0	91 196.807	1.85×10^{-8}	32.0
	27 14 14 0 0 - 26 17 9 0 0	91 250.365	2.62×10^{-9}	325.9
	6 3 3 0 0 - 5 4 2 0 0	91 269.118	1.58×10^{-6}	18.9
	21 16 6 0 1 - 21 15 7 0 2	91 299.04	4.57×10^{-6}	220.0
	25 18 7 0 2 - 25 17 8 0 1	91 334.072	5.25×10^{-6}	304.3
	23 15 9 0 0 - 23 13 10 0 0	91 339.865	5.76×10^{-7}	251.5
	30 8 23 0 2 - 31 5 26 0 1	91 340.082	1.66×10^{-9}	333.7
	30 7 23 0 2 - 31 6 26 0 1	91 340.082	1.66×10^{-9}	333.7
	17 12 5 0 0 - 17 10 7 0 0	91 354.78	8.80×10^{-8}	142.6
	16 7 9 0 2 - 16 7 10 0 1	91 372.165	7.96×10^{-7}	115.0
	16 7 9 0 2 - 16 6 10 0 1	91 380.62	4.25×10^{-6}	115.0
	21 14 8 0 1 - 21 12 9 0 2	91 402.908	4.92×10^{-7}	211.6
	5 3 3 0 0 - 4 1 3 0 0	103 295.419	3.09×10^{-9}	13.2
	37 13 24 0 1 - 36 16 21 0 2	103 296.257	1.76×10^{-8}	557.0
	37 14 24 0 1 - 36 16 21 0 2	103 296.257	4.57×10^{-9}	557.0
	37 14 24 0 1 - 36 15 21 0 2	103 296.268	1.76×10^{-8}	557.0
	37 13 24 0 1 - 36 15 21 0 2	103 296.268	4.57×10^{-9}	557.0
	46 30 16 0 0 - 46 29 17 0 0	103 322.329	1.03×10^{-5}	987.8
	39 26 13 0 2 - 39 25 14 0 1	103 324.61	9.26×10^{-6}	716.2
	17 13 4 0 0 - 16 15 1 0 0	103 347.172	1.82×10^{-9}	145.9
	25 15 11 0 2 - 25 13 12 0 1	103 356.352	1.15×10^{-6}	290.6
	14 4 10 0 0 - 14 4 11 0 0	103 356.454	8.11×10^{-7}	80.3
	14 4 10 0 0 - 14 3 11 0 0	103 356.459	4.22×10^{-6}	80.3
	14 5 10 0 0 - 14 4 11 0 0	103 356.671	4.22×10^{-6}	80.3
	14 5 10 0 0 - 14 3 11 0 0	103 356.676	8.11×10^{-7}	80.3
	23 18 6 0 0 - 23 17 7 0 0	103 357.115	6.18×10^{-6}	264.9
	37 25 12 0 0 - 37 24 13 0 0	103 369.818	8.93×10^{-6}	647.3
	24 9 15 0 2 - 23 11 12 0 1	103 397.728	6.75×10^{-9}	242.8
	24 10 15 0 2 - 23 11 12 0 1	103 397.836	2.84×10^{-8}	242.8
	30 20 11 0 0 - 30 19 12 0 0	103 402.047	8.44×10^{-6}	426.4
	38 10 29 0 0 - 39 7 32 0 0	103 406.702	2.41×10^{-9}	531.8
	38 9 29 0 0 - 39 8 32 0 0	103 406.702	2.41×10^{-9}	531.8
	4 2 2 0 0 - 3 1 3 0 0	103 412.258	5.21×10^{-7}	9.3
	18 14 5 0 0 - 17 16 2 0 0	103 452.707	1.38×10^{-9}	163.5
	6 4 2 0 1 - 5 4 1 0 2	103 468.297	2.68×10^{-6}	19.3
	15 5 10 0 1 - 15 5 11 0 2	103 469.421	9.90×10^{-7}	94.9
	15 5 10 0 1 - 15 4 11 0 2	103 469.491	4.83×10^{-6}	94.9
	15 6 10 0 1 - 15 5 11 0 2	103 471.5	4.83×10^{-6}	94.9
	15 6 10 0 1 - 15 4 11 0 2	103 471.57	9.90×10^{-7}	94.9
	34 24 11 0 0 - 33 27 6 0 0	103 481.533	2.07×10^{-9}	553.7
	4 2 2 0 0 - 3 0 3 0 0	103 486.332	1.19×10^{-7}	9.3

Table B.2: continued.

Species	Transition J K L M	Frequency (MHz)	A_{ij} (s^{-1})	E_{up} (K)
CH_2OHCHO	11 2 10 - 11 1 11	90 591.344	5.85×10^{-6}	38.2
	4 2 2 - 3 1 3	90 785.464	6.54×10^{-6}	8.0
	11 4 8 - 11 3 9	90 922.214	1.24×10^{-5}	46.5
	32 11 22 - 31 12 19	90 940.226	2.43×10^{-6}	368.0
	32 11 21 - 31 12 20	90 977.093	2.43×10^{-6}	368.0
	43 16 28 - 42 17 25	91 277.849	2.30×10^{-6}	682.0
	43 16 27 - 42 17 26	91 277.921	2.30×10^{-6}	682.0
	10 0 10 - 9 1 9	103 391.285	2.79×10^{-5}	28.3
	15 4 12 - 15 3 13	103 461.311	1.78×10^{-5}	76.8
$^{13}CH_2OHCHO$	49 19 31 - 48 20 28	90 623.698	2.17×10^{-6}	891.0
	49 19 30 - 48 20 29	90 623.7	2.17×10^{-6}	891.0
	23 5 18 - 23 4 19	90 629.152	1.69×10^{-5}	171.7
	24 6 18 - 24 5 19	90 745.683	1.83×10^{-5}	190.0
	33 20 13 - 34 19 16	90 765.157	1.15×10^{-6}	546.9
	33 20 14 - 34 19 15	90 765.157	1.15×10^{-6}	546.9
	6 4 3 - 7 1 6	90 791.284	1.47×10^{-8}	21.1
	23 3 20 - 24 2 23	90 833.934	7.95×10^{-8}	161.2
	12 3 10 - 12 1 11	91 019.113	9.70×10^{-9}	48.3
	17 3 14 - 17 2 15	91 123.479	1.24×10^{-5}	93.1
	18 13 5 - 19 12 8	91 151.742	7.59×10^{-7}	194.7
	18 13 6 - 19 12 7	91 151.742	7.59×10^{-7}	194.7
	25 6 19 - 25 5 20	91 236.931	1.88×10^{-5}	204.6
	12 4 9 - 12 3 10	91 277.72	1.26×10^{-5}	52.7
	9 7 3 - 8 7 2	103 285.896	1.65×10^{-7}	53.9
	9 7 2 - 8 7 1	103 285.9	1.65×10^{-7}	53.9
	37 13 25 - 36 14 22	103 343.428	3.52×10^{-6}	489.6
	37 13 24 - 36 14 23	103 349.948	3.52×10^{-6}	489.6
	9 6 4 - 8 6 3	103 420.473	2.33×10^{-7}	46.2
	9 6 3 - 8 6 2	103 420.752	2.33×10^{-7}	46.2
	26 8 18 - 25 9 17	103 459.303	3.85×10^{-6}	233.1
	52 8 44 - 53 7 47	103 468.404	2.66×10^{-7}	815.0
CHDOHCHO	8 5 4 - 7 5 3	90 593.937	1.71×10^{-7}	33.1
	22 16 6 - 23 15 9	90 597.888	6.78×10^{-7}	276.4
	22 16 7 - 23 15 8	90 597.888	6.78×10^{-7}	276.4
	8 5 3 - 7 5 2	90 599.345	1.71×10^{-7}	33.1
	3 3 0 - 2 2 1	90 655.047	1.65×10^{-5}	8.2
	8 3 6 - 7 3 5	90 678.44	2.41×10^{-7}	24.5
	46 8 39 - 47 5 42	90 679.401	1.48×10^{-7}	625.6
	17 3 14 - 17 2 15	90 722.053	1.16×10^{-5}	91.2
	20 15 5 - 21 14 8	90 728.937	6.15×10^{-7}	236.2
	20 15 6 - 21 14 7	90 728.937	6.15×10^{-7}	236.2
	23 5 18 - 23 4 19	90 751.425	1.59×10^{-5}	168.3
	9 0 9 - 8 1 8	90 833.314	1.85×10^{-5}	22.7
	18 14 4 - 19 13 7	90 851.935	5.40×10^{-7}	199.3
	18 14 5 - 19 13 6	90 851.935	5.40×10^{-7}	199.3
	8 4 5 - 7 4 4	90 856.595	2.12×10^{-7}	28.3
	16 13 3 - 17 12 6	90 964.082	4.53×10^{-7}	165.7
	16 13 4 - 17 12 5	90 964.082	4.53×10^{-7}	165.7
	20 4 16 - 20 3 17	91 001.685	1.40×10^{-5}	126.9
	8 4 4 - 7 4 3	91 021.872	2.13×10^{-7}	28.3
	14 12 2 - 15 11 5	91 062.071	3.52×10^{-7}	135.3
	14 12 3 - 15 11 4	91 062.071	3.52×10^{-7}	135.3
	12 11 1 - 13 10 4	91 141.943	2.36×10^{-7}	108.1
	12 11 2 - 13 10 3	91 141.943	2.36×10^{-7}	108.1
	24 3 21 - 25 2 24	91 154.596	6.48×10^{-8}	170.4
	10 10 1 - 11 9 2	91 198.912	1.11×10^{-7}	84.2

Table B.2: continued.

Species	Transition J K L M	Frequency (MHz)	A_{ij} (s^{-1})	E_{up} (K)
	10 10 0 - 11 9 3	91 198.912	1.11×10^{-7}	84.2
	9 1 9 - 8 1 8	91 353.121	2.83×10^{-7}	22.7
	52 8 44 - 53 7 47	93 165.385	1.71×10^{-7}	797.6
aGg-$(CH_2OH)_2$	8 1 7 1 - 7 1 6 0	90 593.579	1.61×10^{-5}	19.1
	35 8 28 0 - 35 7 28 1	90 635.988	3.82×10^{-7}	343.2
	20 1 19 0 - 19 2 17 1	90 642.19	6.48×10^{-8}	101.7
	14 5 10 1 - 14 4 11 1	90 662.384	2.41×10^{-6}	64.3
	32 11 22 0 - 31 12 20 1	90 674.452	1.02×10^{-7}	319.4
	18 3 16 0 - 17 4 14 1	90 675.102	5.45×10^{-8}	88.0
	32 11 21 0 - 31 12 19 1	90 675.776	1.02×10^{-7}	319.4
	35 23 12 1 - 36 22 15 1	90 680.757	1.66×10^{-7}	569.3
	35 23 13 1 - 36 22 14 1	90 680.757	1.66×10^{-7}	569.3
	11 5 6 0 - 11 4 7 0	90 683.206	1.88×10^{-6}	44.8
	11 5 6 1 - 11 4 7 1	90 686.174	1.97×10^{-6}	45.1
	33 22 11 0 - 34 21 14 0	90 701.431	1.30×10^{-7}	513.0
	33 22 12 0 - 34 21 13 0	90 701.431	1.30×10^{-7}	513.0
	26 4 22 0 - 26 4 23 1	90 726.496	8.82×10^{-7}	184.8
	14 5 10 0 - 14 4 11 0	90 731.469	1.99×10^{-6}	64.0
	15 5 11 0 - 15 4 12 0	90 752.358	2.03×10^{-6}	71.4
	53 10 43 0 - 53 10 44 1	90 785.844	7.06×10^{-7}	762.7
	16 3 14 1 - 16 1 15 0	90 802.123	6.80×10^{-7}	71.5
	33 22 11 1 - 34 21 14 1	90 839.672	1.60×10^{-7}	513.4
	33 22 12 1 - 34 21 13 1	90 839.672	1.60×10^{-7}	513.4
	13 5 9 1 - 13 4 10 1	90 852.643	2.23×10^{-6}	57.4
	13 5 9 0 - 13 4 10 0	90 857.67	1.95×10^{-6}	57.1
	31 21 10 0 - 32 20 13 0	90 864.536	1.26×10^{-7}	460.0
	31 21 11 0 - 32 20 12 0	90 864.536	1.26×10^{-7}	460.0
	15 4 11 1 - 15 3 13 0	90 866.003	2.69×10^{-7}	67.7
	20 5 16 0 - 19 6 14 1	90 918.748	1.89×10^{-7}	116.1
	30 10 21 0 - 29 11 19 1	90 926.845	1.06×10^{-7}	278.1
	30 10 20 0 - 29 11 18 1	90 933.622	1.05×10^{-7}	278.1
	19 4 16 1 - 19 3 17 1	90 968.215	1.86×10^{-6}	101.9
	16 5 12 0 - 16 4 13 0	90 992.142	2.09×10^{-6}	79.4
	58 11 47 0 - 58 11 48 1	90 996.168	6.94×10^{-7}	911.4
	31 21 10 1 - 32 20 13 1	90 996.852	1.54×10^{-7}	460.4
	31 21 11 1 - 32 20 12 1	90 996.852	1.54×10^{-7}	460.4
	17 4 13 0 - 16 5 11 1	91 008.128	2.61×10^{-7}	84.1
	29 20 9 0 - 30 19 12 0	91 025.255	1.20×10^{-7}	410.0
	29 20 10 0 - 30 19 11 0	91 025.255	1.20×10^{-7}	410.0
	39 15 25 1 - 38 16 23 0	91 041.27	8.54×10^{-8}	494.3
	12 5 8 0 - 12 4 9 0	91 067.16	1.92×10^{-6}	50.7
	12 5 8 1 - 12 4 9 1	91 076.809	2.13×10^{-6}	51.0
	25 4 21 0 - 25 3 22 0	91 106.286	2.05×10^{-6}	171.7
	31 7 24 1 - 31 6 25 1	91 112.101	3.06×10^{-6}	270.7
	29 20 9 1 - 30 19 12 1	91 151.433	1.47×10^{-7}	410.3
	29 20 10 1 - 30 19 11 1	91 151.433	1.47×10^{-7}	410.3
	27 19 8 0 - 28 18 11 0	91 182.665	1.14×10^{-7}	362.9
	27 19 9 0 - 28 18 10 0	91 182.665	1.13×10^{-7}	362.9
	14 3 11 1 - 13 4 10 1	91 186.341	6.58×10^{-7}	57.4
	16 3 14 1 - 15 4 12 0	91 213.836	1.30×10^{-7}	71.5
	14 3 11 0 - 13 4 10 0	91 224.675	4.15×10^{-7}	57.1
	28 9 20 0 - 27 10 18 1	91 234.81	1.11×10^{-7}	239.8
	10 5 5 0 - 10 4 6 0	91 244.026	1.81×10^{-6}	39.3
	10 5 5 1 - 10 4 6 1	91 253.037	1.92×10^{-6}	39.7
	28 9 19 0 - 27 10 17 1	91 267.756	1.10×10^{-7}	239.8
	27 19 8 1 - 28 18 11 1	91 302.508	1.39×10^{-7}	363.2

Table B.2: continued.

Species	Transition J K L M	Frequency (MHz)	A_{ij} (s^{-1})	E_{up} (K)
	27 19 9 1 - 28 18 10 1	91 302.508	1.39×10^{-7}	363.2
	11 5 7 0 - 11 4 8 0	91 308.601	1.87×10^{-6}	44.7
	11 5 7 1 - 11 4 8 1	91 321.795	2.05×10^{-6}	45.1
	16 5 12 1 - 16 4 13 1	91 327.482	1.50×10^{-6}	79.7
	25 18 7 0 - 26 17 10 0	91 335.784	1.06×10^{-7}	318.7
	25 18 8 0 - 26 17 9 0	91 335.784	1.06×10^{-7}	318.7
	18 4 15 1 - 17 5 12 1	91 340.39	4.62×10^{-7}	92.6
	37 14 24 1 - 36 15 22 0	91 349.668	8.79×10^{-8}	442.3
	37 14 23 1 - 36 15 21 0	91 349.672	8.79×10^{-8}	442.3
	15 1 14 1 - 15 1 15 0	93 180.613	3.17×10^{-7}	59.9
	18 2 16 1 - 17 4 14 1	93 181.585	4.49×10^{-8}	88.2
	19 1 18 1 - 18 2 16 0	103 296.497	1.03×10^{-7}	92.8
	25 7 19 0 - 24 8 17 1	103 307.653	2.11×10^{-7}	184.5
	19 2 17 1 - 19 2 18 0	103 341.273	2.55×10^{-7}	97.4
	17 6 11 0 - 17 5 13 1	103 365.434	4.16×10^{-7}	93.1
	15 6 10 0 - 15 5 10 1	103 477.405	5.87×10^{-7}	76.8
	30 10 21 1 - 29 11 19 0	103 489.245	1.47×10^{-7}	278.4
	30 10 20 1 - 29 11 18 0	103 496.358	1.48×10^{-7}	278.4
gGg-$(CH_2OH)_2$	19 2 18 0 - 18 3 16 1	90 619.203	6.90×10^{-7}	91.9
	9 5 4 1 - 9 4 5 1	90 625.64	3.63×10^{-6}	34.2
	9 5 4 0 - 9 4 5 0	90 637.706	3.50×10^{-6}	34.1
	22 6 17 0 - 22 5 17 1	90 710.878	3.12×10^{-6}	141.6
	9 5 5 1 - 9 4 6 1	90 750.006	3.54×10^{-6}	34.2
	9 5 5 0 - 9 4 6 0	90 761.349	3.62×10^{-6}	34.1
	17 3 15 0 - 16 4 13 1	90 849.293	1.24×10^{-6}	78.8
	19 15 4 1 - 20 14 6 0	90 855.162	1.57×10^{-7}	202.0
	19 15 5 1 - 20 14 7 0	90 855.162	1.57×10^{-7}	202.0
	8 5 3 1 - 8 4 4 1	90 862.788	3.34×10^{-6}	29.8
	8 5 3 0 - 8 4 4 0	90 874.028	3.28×10^{-6}	29.7
	8 5 4 1 - 8 4 5 1	90 911.505	3.31×10^{-6}	29.8
	8 5 4 0 - 8 4 5 0	90 922.458	3.32×10^{-6}	29.7
	16 1 15 0 - 16 0 16 0	90 930.932	1.45×10^{-6}	66.7
	11 5 7 1 - 11 4 7 0	90 988.303	3.83×10^{-6}	44.5
	7 5 2 1 - 7 4 3 1	91 016.495	2.96×10^{-6}	25.9
	7 5 2 0 - 7 4 3 0	91 027.312	2.92×10^{-6}	25.8
	7 5 3 1 - 7 4 4 1	91 032.962	2.95×10^{-6}	25.9
	7 5 3 0 - 7 4 4 0	91 043.681	2.93×10^{-6}	25.8
	4 3 2 1 - 3 2 1 1	91 101.828	4.93×10^{-6}	9.3
	6 5 1 1 - 6 4 2 1	91 113.072	2.40×10^{-6}	22.5
	4 3 2 0 - 3 2 1 0	91 113.703	4.72×10^{-6}	9.3
	17 14 3 1 - 18 13 5 0	91 113.915	1.32×10^{-7}	169.9
	17 14 4 1 - 18 13 6 0	91 113.915	1.31×10^{-7}	169.9
	6 5 2 1 - 6 4 3 1	91 117.61	2.39×10^{-6}	22.5
	6 5 1 0 - 6 4 2 0	91 123.664	2.37×10^{-6}	22.4
	17 5 12 0 - 17 4 14 1	91 125.215	4.19×10^{-6}	87.2
	6 5 2 0 - 6 4 3 0	91 128.176	2.37×10^{-6}	22.4
	16 1 15 1 - 16 0 16 1	91 152.424	1.69×10^{-6}	66.8
	5 5 0 1 - 5 4 1 1	91 170.801	1.52×10^{-6}	19.5
	5 5 1 1 - 5 4 2 1	91 171.716	1.52×10^{-6}	19.5
	41 6 35 1 - 40 9 32 1	91 177.349	1.31×10^{-7}	446.6
	5 5 0 0 - 5 4 1 0	91 181.28	1.50×10^{-6}	19.5
	5 5 1 0 - 5 4 2 0	91 182.189	1.50×10^{-6}	19.5
	30 5 25 0 - 30 5 26 1	91 231.701	3.36×10^{-7}	244.5
	41 6 35 0 - 40 9 32 0	91 257.694	1.21×10^{-7}	446.6
	18 5 14 1 - 18 4 15 1	91 262.747	4.24×10^{-6}	96.0
	18 5 14 0 - 18 4 15 0	91 268.437	4.70×10^{-6}	96.0

Table B.2: continued.

Species	Transition J K L M	Frequency (MHz)	A_{ij} (s^{-1})	E_{up} (K)
	13 5 8 1 - 13 4 10 0	91 275.54	3.05×10^{-6}	56.7
	14 5 9 1 - 14 4 11 0	91 280.948	3.02×10^{-6}	63.6
	18 3 16 0 - 18 1 17 1	91 306.616	1.57×10^{-6}	87.5
	9 2 8 1 - 8 2 7 0	91 332.324	6.59×10^{-6}	23.8
	31 7 24 1 - 31 6 25 1	91 355.815	6.00×10^{-6}	268.3
	15 13 2 1 - 16 12 4 0	91 361.122	1.01×10^{-7}	140.7
	15 13 3 1 - 16 12 5 0	91 361.122	1.01×10^{-7}	140.7
	9 4 5 1 - 8 4 4 0	93 162.746	5.77×10^{-6}	29.8
	17 3 15 1 - 16 4 13 0	93 172.871	1.32×10^{-6}	78.9
	18 5 13 0 - 18 4 15 1	93 190.697	3.45×10^{-6}	96.1
	10 4 7 1 - 9 4 6 0	103 372.306	8.30×10^{-6}	34.7
	18 4 14 0 - 18 3 16 1	103 426.616	1.89×10^{-6}	92.5
	22 4 19 0 - 22 2 20 1	103 438.467	5.12×10^{-6}	131.6
	22 2 21 0 - 21 2 19 0	103 457.183	1.01×10^{-7}	121.0
	19 3 17 0 - 18 4 15 1	103 488.002	1.74×10^{-6}	96.6
D_2CO	5 1 4 - 5 1 5	91 246.233	1.61×10^{-6}	49.6
t-HCOOH	34 4 30 - 34 4 31	103 423.53	2.60×10^{-7}	700.5
c-C_2H_4O	11 6 5 - 11 5 6	90 842.056	8.21×10^{-6}	137.2
	21 14 7 - 21 13 8	91 160.793	1.21×10^{-5}	492.8
c-C_2H_3DO	9 5 5 - 9 3 6	90 667.609	1.17×10^{-7}	83.6
	7 2 5 - 7 2 6	90 683.057	9.45×10^{-8}	48.3
	7 2 5 - 7 1 6	90 710.475	4.70×10^{-6}	48.3
	10 8 2 - 10 7 3	90 781.87	6.42×10^{-6}	113.1
	13 8 6 - 12 11 1	90 852.748	1.17×10^{-9}	174.4
	12 7 6 - 11 10 1	91 140.581	1.69×10^{-9}	147.5
	13 2 11 - 12 5 8	91 153.128	1.10×10^{-8}	141.1
	13 3 11 - 12 4 8	91 366.508	1.10×10^{-8}	141.1
HC_3N	10 - 9	90 979.023	5.81×10^{-5}	24.0
CH_3CH_2CN	35 5 31 - 36 2 34	90 800.771	6.07×10^{-8}	299.2
	49 7 43 - 50 5 46	90 949.453	2.17×10^{-8}	581.9
	58 8 51 - 59 6 54	90 998.392	2.24×10^{-8}	807.6
	27 2 25 - 27 2 26	91 008.34	5.49×10^{-7}	169.8
	29 3 26 - 29 2 27	91 018.22	5.25×10^{-6}	199.1
	48 7 41 - 47 8 40	91 161.765	1.09×10^{-6}	560.8
	61 3 58 - 60 5 55	91 196.7	3.17×10^{-8}	828.0
	36 2 34 - 35 4 31	91 281.468	7.96×10^{-8}	294.8
	35 3 33 - 36 1 36	91 284.048	5.56×10^{-9}	280.5
	14 3 12 - 15 0 15	91 342.464	3.11×10^{-8}	55.2
	35 3 33 - 36 0 36	91 350.299	2.83×10^{-8}	280.5
	39 2 37 - 40 1 40	93 156.345	2.49×10^{-8}	343.8
	39 2 37 - 40 0 40	93 181.535	4.84×10^{-9}	343.8
	21 7 15 - 22 6 16	103 384.573	1.23×10^{-6}	153.8
	21 7 14 - 22 6 17	103 385.42	1.23×10^{-6}	153.8
	60 4 57 - 59 5 54	103 417.147	2.63×10^{-7}	802.3
$HOCH_2CN$	38 2 36 0 - 39 1 39 0	90 597.603	5.26×10^{-8}	338.5
	25 2 23 0 - 25 1 24 0	90 619.344	4.38×10^{-6}	151.6
	18 4 14 0 - 18 3 16 1	90 635.379	2.87×10^{-6}	98.0
	36 8 29 0 - 37 7 30 0	90 753.122	1.17×10^{-6}	383.8
	36 8 28 0 - 37 7 31 0	90 757.105	1.17×10^{-6}	383.8
	19 4 15 0 - 19 3 17 1	90 808.881	2.86×10^{-6}	106.4
	49 5 45 1 - 50 2 48 1	90 829.279	8.35×10^{-8}	583.4
	23 4 19 1 - 24 2 22 1	90 918.82	1.95×10^{-7}	149.9
	29 5 25 1 - 30 4 27 0	90 932.471	1.27×10^{-6}	232.8
	23 2 21 0 - 23 1 23 1	90 938.751	8.97×10^{-7}	129.5
	8 0 8 1 - 8 1 8 0	90 948.488	6.84×10^{-6}	21.3
	8 1 8 1 - 7 2 6 0	90 973.549	8.01×10^{-7}	22.3

Table B.2: continued.

Species	Transition J K L M	Frequency (MHz)	A_{ij} (s^{-1})	E_{up} (K)
	20 4 16 0 - 20 3 18 1	91 039.63	2.87×10^{-6}	115.3
	42 2 40 0 - 41 4 37 0	91 089.387	1.69×10^{-7}	410.4
	56 7 50 1 - 55 8 47 1	91 170.271	1.30×10^{-6}	780.4
	49 5 45 0 - 50 2 48 0	91 212.431	1.20×10^{-7}	578.4
	10 0 10 1 - 9 0 9 1	91 244.602	2.25×10^{-5}	29.6
	35 6 30 1 - 36 5 32 0	91 280.978	1.27×10^{-6}	334.4
	10 0 10 0 - 9 0 9 0	91 282.104	2.27×10^{-5}	24.2
	29 2 27 1 - 29 2 28 1	91 307.51	1.12×10^{-7}	206.3
	21 4 17 0 - 21 3 19 1	91 343.484	2.87×10^{-6}	124.6
	34 3 32 0 - 33 4 29 0	93 175.688	1.03×10^{-6}	276.0
	16 1 15 0 - 15 1 15 1	93 179.831	4.57×10^{-7}	62.8
	30 9 21 0 - 31 8 23 1	93 190.634	9.50×10^{-7}	318.3
	30 9 22 0 - 31 8 24 1	93 190.64	9.50×10^{-7}	318.3
	35 2 33 0 - 34 3 31 1	103 318.063	3.15×10^{-6}	288.9
	45 3 42 1 - 45 3 42 0	103 318.312	9.15×10^{-8}	482.2
	59 9 51 1 - 58 10 49 0	103 334.357	1.76×10^{-6}	901.2
	59 9 50 1 - 58 10 48 0	103 341.424	1.76×10^{-6}	901.2
	20 2 18 0 - 19 2 18 1	103 352.311	7.48×10^{-8}	99.7
	21 4 17 1 - 22 3 19 0	103 384.207	1.71×10^{-6}	130.0
	32 2 30 1 - 32 2 30 0	103 402.141	1.77×10^{-6}	248.2
	27 4 23 1 - 26 5 21 0	103 421.493	1.71×10^{-6}	195.2
	57 7 50 0 - 56 8 49 0	103 437.673	1.87×10^{-6}	800.8
	46 8 38 1 - 47 7 40 0	103 440.794	1.79×10^{-6}	572.8
	48 4 44 1 - 48 4 44 0	103 506.105	1.08×10^{-7}	552.9
NH_2CHO	15 3 12 - 16 1 15	91 136.103	4.85×10^{-8}	149.5
	36 5 32 - 35 6 29	103 296.485	7.38×10^{-7}	755.7
	20 5 16 - 21 4 17	103 446.144	7.16×10^{-7}	288.6
CH_3SH	1 -1 1 1 - 0 0 0 1	90 637.359	7.97×10^{-7}	5.8
	12 -1 12 4 - 11 -2 10 4	91 128.19	3.80×10^{-7}	571.2
	9 1 8 1 - 9 0 9 1	103 389.812	2.55×10^{-6}	61.0
	12 3 9 1 - 13 2 11 1	103 399.789	5.79×10^{-7}	133.6
	8 0 8 0 - 7 1 6 0	103 504.193	1.54×10^{-6}	43.7
	27 5 22 -3 - 26 6 20 -3	103 508.935	5.40×10^{-7}	870.7
	27 -5 23 -3 - 26 -6 21 -3	103 509.321	5.40×10^{-7}	870.7